Quasi-Periodic Energy Release in a Three-Ribbon Solar Flare

Ivan Zimovets[1] · Ivan Sharykin[1] · Ivan Myshyakov[2]

Abstract

Quasi-periodic pulsations (QPPs) are found in solar flares of various magnetic morphologies, e.g. in two-ribbon or circular-ribbon flares, and the mechanisms of their generation are not yet clear. Here we present the first detailed analysis of QPPs (with a period $P = 54 \pm 13$ seconds) found in the *Ramaty High Energy Solar Spectroscopic Imager* (RHESSI) observations of a relatively rare three-ribbon M1.1 class flare that occurred on 5 July 2012 (SOL2012-07-05T06:49). QPPs are manifested in the temporal profiles of temperature [T] and emission measure [EM] of "super-hot" ($T_s \approx 30 - 50$ MK) plasma but are almost invisible in the profiles of "hot" ($T_h \approx 15 - 20$ MK) plasma parameters when approximating X-ray spectra of the flare with the bremsstrahlung spectrum of a two-temperature thermal (Maxwellian) plasma. In addition, QPPs with a similar period are found in the temporal profiles of the flux and spectral index of nonthermal electrons if the observed X-ray spectra are approximated by a combination of the bremsstrahlung spectra of a single-temperature plasma and nonthermal electrons with a power-law energy distribution. QPPs are not well expressed in the X-ray flux according to RHESSI and GOES data, or in radio data. The QPPs are accompanied by apparent systematic movement of a single X-ray source at a low speed of 34 ± 21 km s^{-1} along the central flare ribbon over a narrow (< 5 Mm) "tongue" of negative magnetic polarity, elongated (≈ 20 Mm) between two areas of positive polarity. The results of magnetic extrapolation in the nonlinear force-free field (NLFFF) approximation show that the X-ray source could move along curved and twisted field lines between two sheared flare arcades. It is worth noting that in the homologous three-ribbon M6.1 flare (SOL2012-07-05T11:39), which occurred in the same region about five hours later, the X-ray sources moved much less systematically and did not produce similar QPPs. We interpret the observed QPPs as a result of successive episodes of energy release in different spatial locations. In each pulsation, $\approx (1 - 4) \times 10^{29}$ erg is released in the form of thermal energy of hot and super-hot plasmas (or accelerated electrons), which is comparable with the energy of a microflare. The total kinetic energy released during all QPPs is $\approx (0.7 - 3.5) \times 10^{30}$ erg, which is about an order of magnitude less than the free magnetic energy $\approx 1.56 \times 10^{31}$ erg released in the flare region. We discuss possible propagating triggers of the quasi-periodic energy release (slow magnetoacoustic waves, asymmetric rise of curved/twisted field lines, flapping oscillations, and thermal instability in a reconnecting current sheet) and argue that

Extended author information available on the last page of the article

🍀 Springer

the current state of available mechanisms and observations does not allow us to reach an unambiguous conclusion.

1. Introduction

Solar flares are one of the most powerful phenomena of solar activity. They represent sporadic, short-term (minutes – hours) episodes of transformation of free magnetic energy into other types of energy – kinetic energy of accelerated particles, the thermal and mechanical energy of plasma, various types of waves, and in particular electromagnetic radiation in a wide spectral range, from radio waves to γ-rays (e.g. Fletcher et al., 2011; Benz, 2017). Thanks to this radiation, we have the opportunity to observe and study flares occurring on the Sun.

The emission temporal profiles (light curves) of many flares exhibit quasi-periodic pulsations (QPPs). In recent years, several statistical studies have been carried out in order to determine the frequency of occurrence of QPPs in flares (Simões, Hudson, and Fletcher, 2015; Inglis et al., 2016; Pugh et al., 2017; Dominique et al., 2018; Pugh, Broomhall, and Nakariakov, 2019; Hayes et al., 2020). Different works show different results – QPPs are found in 20% to 90% of flares. The results depend on the data analyzed and the methods used to determine the presence of QPPs (Broomhall et al., 2019). It becomes clear that QPPs occur in a large fraction of flares, and their study is important for a general understanding of flares. In addition, if the mechanism(s) of QPPs is reliably determined, their observed properties can provide useful information on the physical characteristics of the flare regions. This direction can be called QPP-diagnostics of solar and stellar flares. For the reasons mentioned, the study of QPPs has been actively developed in recent years, and information about these studies can be found in several reviews (Nakariakov and Melnikov, 2009; Nakariakov et al., 2010; Van Doorsselaere, Kupriyanova, and Yuan, 2016; McLaughlin et al., 2018; Kupriyanova et al., 2020; Zimovets et al., 2021).

More than a dozen different QPP mechanisms in flares are currently being discussed, and two classifications have been proposed recently. According to McLaughlin et al. (2018), all mechanisms can be divided into three groups: i) oscillatory, ii) self-oscillatory, and iii) autowave processes. Kupriyanova et al. (2020) proposed a different classification: i) direct emission modulation by magnetohydrodynamic (MHD) and electrodynamic oscillations of all types, ii) periodic modulation, via MHD oscillations, of the efficiency of energy release processes such as magnetic reconnection, and iii) spontaneous quasi-periodic energy release. Both classifications have the right to exist, and now it is difficult to conclude which one is preferable (see the review by Zimovets et al., 2021, where this issue is discussed). The emergence of these classifications, on the one hand, indicates a certain systematization of knowledge about the QPPs and maturation of this research field. On the other hand, it highlights the need for the development of a classification of all types of QPPs based on observational characteristics, similar to how it is done, e.g., for geomagnetic pulsations in the Earth's magnetosphere (e.g. see the review by Nakariakov et al., 2016).

Moving in this direction, recently several studies have attempted to find relationships between some properties of QPPs (mainly their period) and various parameters of the parent active regions. In particular, Pugh, Broomhall, and Nakariakov (2019) found correlations between QPPs' period and several parameters of the flare ribbons. The strongest correlations

are between QPPs' period and flare-ribbon area, total unsigned magnetic flux below the ribbons, and ribbon-separation distance. Hayes et al. (2020) have confirmed these results by applying different QPP detection techniques to a much larger sample of flares. These results indicate the presence of some (so far not obvious) connections between parameters of QPPs and flare ribbons.

QPPs have been observed and studied in detail in solar flares differing in magnetic configuration, number, or geometry of flare ribbons (usually observed in the UV and optical ranges, particularly in the Hα line). There are works devoted to the study of QPPs in two-ribbon flares (e.g. Zimovets and Struminsky, 2009; Inglis and Dennis, 2012; Brosius, Daw, and Inglis, 2016), in circular or quasi-circular-ribbon flares (e.g. Kumar, Nakariakov, and Cho, 2016; Zhang, Li, and Ning, 2016; Chen et al., 2019; Kashapova et al., 2020), and in flares with more complex geometries and arrangement of flare loops (e.g. Grechnev, White, and Kundu, 2003; Zimovets and Struminsky, 2010; Li and Zhang, 2015; Li, Ning, and Zhang, 2015). There is also another group of flares: the three-ribbon flares (e.g. Wang et al., 2014; Grechnev et al., 2020). They are relatively rarer, and we are not aware of any works that would provide a detailed analysis of the observations of QPPs in such events.

The existence of flares differing in number and geometry of flare ribbons indicates the presence of various 3D magnetic configurations. The most common two-ribbon flares usually occur in a bipolar magnetic configuration and are mainly interpreted by the "standard" flare model (e.g. see the reviews by Priest and Forbes, 2002; Shibata and Magara, 2011; Janvier, Aulanier, and Démoulin, 2015, and references therein). Within its framework, a magnetic-flux rope forms, experiences instability, and rises upward, pulling out the surrounding magnetic-field lines, usually in the form of an arcade of magnetic loops. A current sheet forms under the erupting flux rope, and magnetic reconnection happens in it, leading to plasma heating and acceleration of charged particles. A part of them goes down (probably experiencing additional energization on the way) to the feet of the arcade loops and heats the plasma there, which can be seen in the form of a pair of flare ribbons expanding from the magnetic polarity inversion line (PIL). Hard X-ray sources (due to the bremsstrahlung of non-thermal electrons in the chromosphere) in the form of ribbons are also sometimes observed, but more often in the form of separate compact X-ray footpoints (see the review by Fletcher et al., 2011). Most of the known QPP mechanisms can be incorporated into the standard flare model to interpret the observed QPPs in a particular event.

Circular-ribbon flares usually occur in active regions where a parasitic magnetic polarity is rooted inside the primary magnetic polarity. A fan–spine magnetic topology is usually assumed (e.g. Masson et al., 2009; Sun et al., 2013). The fan has a dome shape, and the chromospheric footpoints of field lines, which belong to the closed separatrix surface, correspond to the circular flare ribbons. The spine field lines go through a null-point (presumably in the corona). Their inner ends correspond to the inner flare brightenings/ribbon. When the outer spine field lines are "open", reconnection around the null-point can cause coronal jets or surges (Pariat, Antiochos, and DeVore, 2010). Another situation occurs when the outer spine field lines are closed (to the photosphere). In this case, the slip-running reconnection in the quasi-separatrix layers (QSLs) near the null-point can cause sequential brightenings of the circular ribbons, while the following reconnection in the null-point can be associated with the formation of the remote brightenings/ribbons (Masson et al., 2009). To interpret the QPPs in the circular-ribbon flares, it is often assumed that the magnetic reconnection in the vicinity of the null-point occurs in a quasi-periodic regime (Zhang, Li, and Ning, 2016; Chen et al., 2019; Kashapova et al., 2020). In particular, the quasi-periodic slip-running reconnection could be assumed to interpret the sequential appearance of brightenings in the circular ribbons associated with the QPPs. Other mechanisms could also be used to interpret the

QPPs in some specific cases. For example, Kumar, Nakariakov, and Cho (2016) interpreted the QPPs with a period of around three minutes as a result of quasi-periodic modulation of reconnection in a coronal null-point by the three-minute slow-mode waves from nearby sunspot oscillations or by untwisting, three-minute motions of a filament.

As mentioned above, three-ribbon flares are much less common. There are only a few works in the literature devoted to the analysis of such events. In particular, Wang et al. (2014) have made a detailed study of two homologous three-ribbon flares of M1.9 and C9.2 classes that happened in the same NOAA Active Region 11515 on 6 July 2012 (SOL2012-07-06T18:48 and SOL2012-07-06T19:20, respectively). It was shown that in both flares, the two outer ribbons (R_1 and R_3) were located in the regions of positive magnetic polarity and the central ribbon (R_2) was in an elongated "tongue" of negative magnetic polarity, sandwiched between two regions of positive polarity in the North and in the South. Observations and extrapolation of magnetic field in the nonlinear force-free field (NLFFF) approximation showed that the northern and central (R_1 and R_2), and southern and central (R_3 and R_2) flare ribbons were connected by two systems of sheared magnetic loops, and the overall magnetic geometry resembled an asymmetric fish-bone-like structure. This magnetic system was surrounded by field lines connecting the main flare area with the area of remote brightenings. A series of jets/surges were observed along these field lines. An interesting observational finding is the sequential brightenings and elongation of the outer ribbons as well as the displacement of hard X-ray sources during the flares. To interpret the observations, Wang et al. (2014) proposed that the magnetic structure in these three-ribbon flares resembles in many ways the structure of circular-ribbon flares, with the difference that in the three-ribbon flares, there is a translational (2.5D) symmetry along two PILs running on different sides of the elongated, central magnetic polarity. In this case, the coronal magnetic null-point is replaced by a null-line, along which a current sheet can be induced and magnetic reconnection proceeds in the course of the flare.

On the other hand, Grechnev et al. (2020), based on the analysis of two other, more powerful, homologous three-ribbon flares (M7.6 SOL2016-07-23T05:00 and M5.5 SOL2016-07-23T05:27), came to the conclusion that the energy release in these flares, similarly to how it occurs in two-ribbon flares, could be initiated by the eruption of magnetic-flux ropes. The difference is that the main reconnecting current sheet is formed not under the flux rope, but in the vicinity of the coronal null-point (or the null-line in 3D), due to changes in the magnetic field as a response to the flux-rope eruption. The first eruption causes the first flare and prepares conditions for the second eruption, which, in turn, initiates the second flare.

From these two works by Wang et al. (2014) and Grechnev et al. (2020), it can be seen that although the general magnetic topology of three-ribbon flares is becoming known, the details of what exactly is the trigger of the energy release and how exactly reconnection occurs in a complex three-dimensional geometry remain not completely clear. In this article, we present a detailed analysis of one three-ribbon solar flare (M1.1 class SOL2012-07-05T06:49) that occurred in the same NOAA Active Region 11515 in which the three-ribbon flares studied by Wang et al. (2014) were observed (Section 2.1). This flare is of interest because we found signs of quasi-periodic energy release in the *Ramaty High-Energy Solar Spectroscopic Imager* (RHESSI: Lin et al., 2002) data during it (Section 2.2) and had the opportunity to study the location and dynamics of their sources relative to the flare ribbons (Section 2.3) and magnetic-field lines in the corona (Section 2.4). We also had the opportunity to compare the dynamics of X-ray sources in this M1.1 flare and in another homologous three-ribbon flare (M6.1, SOL2012-07-05T11:39) that occurred in the same active region approximately five hours later (Section 2.3). Spatially resolved observations of QPPs' sources are important because they provide constraints on the possible physical

mechanisms of energy release (see Zimovets et al., 2021). This issue is discussed in Section 3, and we make our conclusions in Section 4. There is also an Appendix where we argue that the quasi-periodic variations of the fitting parameters could not be due to a known artifact in the RHESSI data.

2. Analysis of Observations

2.1. General Overview of the Flare Region

The NOAA Active Region 11515 was very flare-productive. It produced more than one hundred flares during its passage across the visible solar hemisphere from 27 June to 10 July 2012. Most of the flares were C-class ($\approx 76\%$), M-class flares accounted for $\approx 24\%$, and there was only one X-class (X1.1) flare, which, most likely, began in the nearby Active Region NOAA 11514 and spread to Active Region 11515. Thus, most likely, the free magnetic energy in Active Region 11515 was effectively dumped through numerous flares of C and M classes and did not accumulate to very high values. More information about this active region has been given by Song et al. (2018), where the relationships between white-light flares and magnetic transients on the photosphere have been studied.

There were at least eight M-class flares in NOAA Active Region 11515 on 5 July 2012 (according to solarmonitor.org/). The temporal profiles of solar X-ray emission detected by the *X-Ray Sensor* (XRS: e.g. Garcia, 1994) onboard the *Geostationary Operational Environmental Satellite* (GOES) and RHESSI during this day are shown in Figures 1a and 1b, respectively. From these eight flares, RHESSI made good detections of only three: M4.7 (SOL2012-07-05T03:25), M1.1 (SOL2012-07-05T06:49), and M6.1 (SOL2012-07-05T11:39). The last two had very similar evolution of their X-ray light curves, which are compared in Figures 1c,e and 1d,f. It can be seen that although the M1.1 flare was less powerful than M6.1 and did not show detectable hard X-ray emission above ≈ 50 keV, both of these flares had two main episodes of energy release on the same temporal scale (both of these flares lasted for ≈ 20 minutes). In this work, we focus on the M1.1 flare analysis and pay only a little attention to the M6.1 flare, which we use for comparison of dynamics of X-ray sources later (Section 2.3.1).

Both of these flares, M1.1 and M6.1, were homologous three-ribbon flares that happened almost in the same place within the active region (taking into account the rotation of the Sun). Figure 2 shows images of the M1.1 flare region made around the first flare X-ray peak, which is indicated by two vertical dotted lines in Figure 1c,e. Three flare ribbons, denoted as the south (FR_S), central (FR_C), and north (FR_N) ribbons, are well seen in the images made by the *Atmospheric Imaging Assembly* (AIA: Lemen et al., 2012) onboard the *Solar Dynamics Observatory* (SDO) in the 1600 Å and 1700 Å ultraviolet (UV) channels. These three ribbons are also well seen in the Ca II H line images of the *Solar Optical Telescope* (SOT: Tsuneta et al., 2008) onboard *Hinode* (not shown here).

Comparison of Figures 2a,b and Figure 2c shows that the central flare ribbon, FR_C, was located in the narrow ($\approx 1 - 10$ Mm) "tongue" of negative magnetic polarity elongated from East to West. It was sandwiched from the South and North by areas of positive magnetic polarity, where, along two PILs, the South and North flare ribbons were located. The west part of the north flare ribbon had a hook-like bend northward. In Figure 2c, we overplotted the flare-region map of the line-of-sight magnetic-field component [B_{LOS}], with the iso-contours of positive and negative vertical (radial) electric-current density j_r (above three standard deviations for a background region outside strong magnetic fields), calculated from
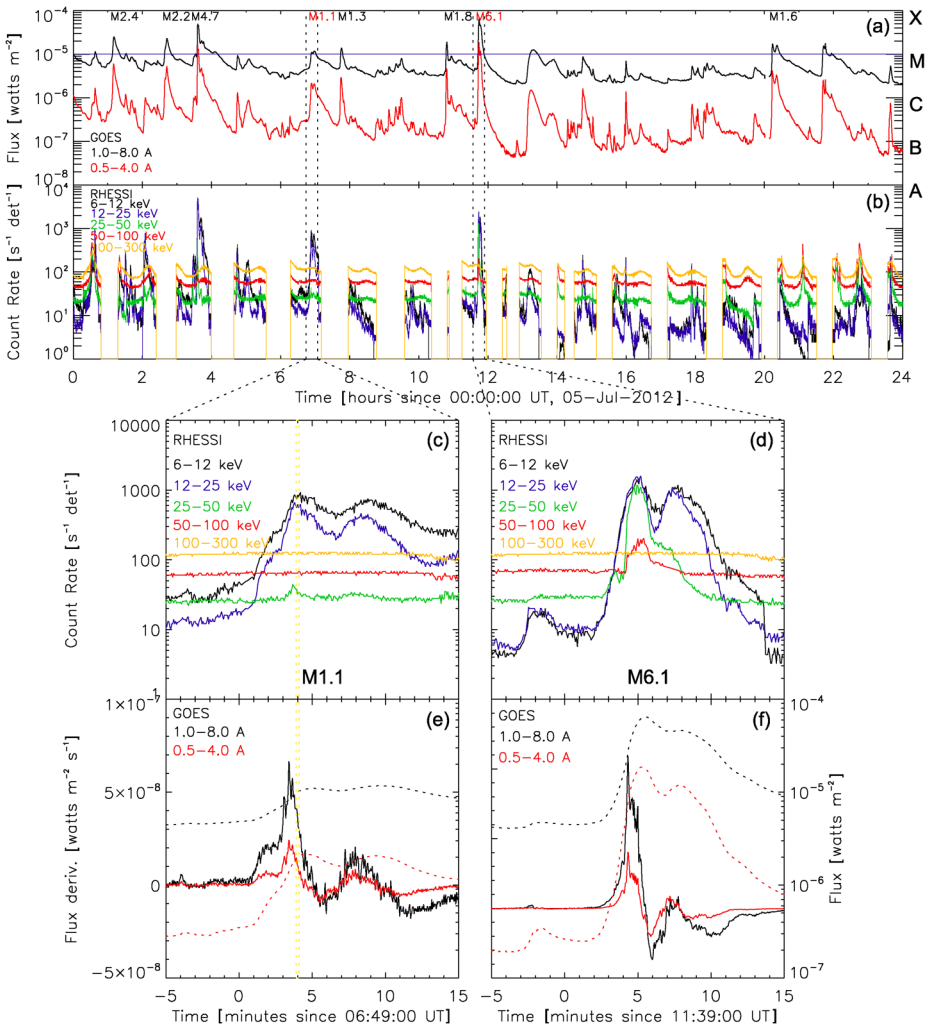
Figure 1 Temporal profiles of solar X-ray emission on 5 July 2012. (**a**) X-ray flux detected by GOES in the 1−8 Å (*black*) and 0.5−1 Å (*red*) channels. (**b**) Corrected count rates averaged over RHESSI's detectors in five energy bands: 6−12 keV (*black*), 12−25 keV (*blue*), 25−50 keV (*green*), 50−100 keV (*red*), and 100−300 keV (*orange*). The M1.1 (SOL2012-07-05T06:49) and M6.1 (SOL2012-07-05T11:39) flares studied in this work are marked with *the vertical dotted lines*. RHESSI's corrected count rates for the 20-minute time intervals around these flares are shown in (**c**) and (**d**), respectively. X-ray fluxes detected by GOES (*dotted curves*) and their first temporal derivatives (*solid curves*) are shown in (**e**) and (**f**).

the pre-flare 720-second photospheric vector magnetograms of the *Helioseismic and Magnetic Imager* (HMI: Scherrer et al., 2012) onboard SDO using the same technique by in Zimovets, Sharykin, and Gan (2020). From this, one can see that the flare ribbons approximately coincided with the elongated regions of enhanced vertical currents (current ribbons) on the photosphere. The south flare ribbons coincided roughly with positive j_r, the north ribbon with negative j_r, and the central ribbon was located in the regions of both positive and negative j_r in the negative magnetic tongue. The south part of this tongue was occupied
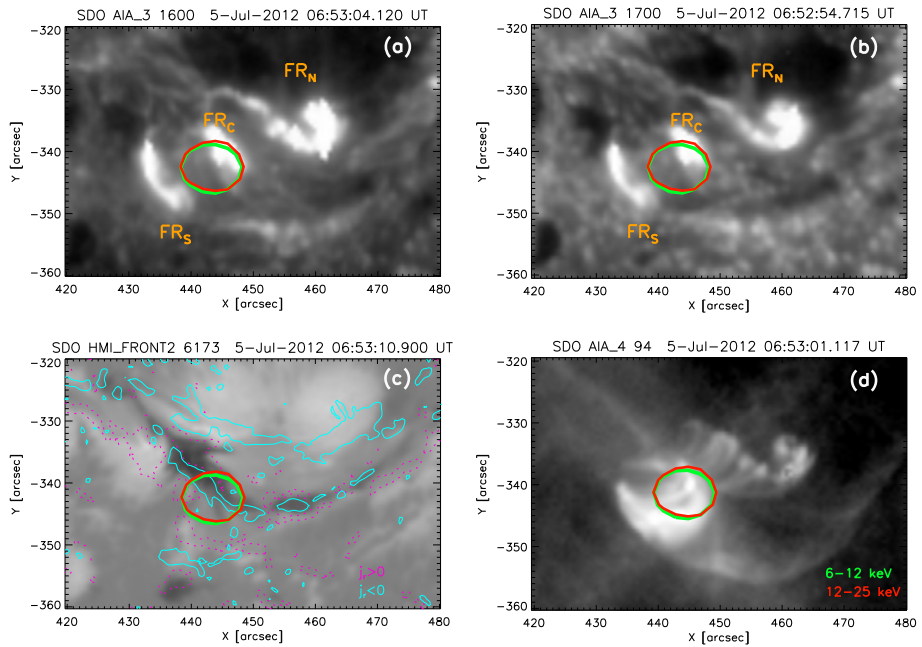
Figure 2 Observations of the M1.1 (SOL2012-07-05T06:49) solar-flare region in the temporal interval near the first X-ray peak indicated by two vertical dotted lines in Figure 1c,e. (**a**) and (**b**) SDO/AIA images in the 1600 Å and 1700 Å channels, respectively. Three flare ribbons (namely the south, center, and north ribbons denoted as FR_S, FR_C, and FR_N, respectively) are seen. (**c**) SDO/HMI map of the line-of-sight magnetic-field component, B_{LOS}, on the photosphere (-2500 G – *black*, $+2500$ G – *white*) overlayed with iso-contours of positive (*dotted pink*) and negative (*solid cyan*) vertical (i.e. radial) electric current density at the levels of $j_r = \pm 7242$ statampere cm^{-2}. (**d**) Image of the flare region made in the "hot" SDO/AIA 94 Å channel. On each panel X-ray sources observed by RHESSI in two energy bands of 6 – 12 keV and 12 – 25 keV are shown with the *green and red iso-contours*, respectively, at the level of 50% from the maximum.

mainly by the negative j_r, while the north part was occupied by the positive j_r – oppositely to the signs of j_r in the nearby south and north flare ribbons. Hence, we can assume that the south ribbon and the south part of the central ribbon, and the north ribbon and the north part of the central ribbon, were connected by two systems of magnetic-field lines with strong ($|j_r| > 7242$ statampere cm^{-2} or ≈ 24 mA m^{-2}) electric currents, i.e. by two arcades of magnetic loops with shear and/or twist (below it will also be confirmed using the NLFFF extrapolation; see Section 2.4). This magnetic structure resembles the fish-bone-like structure found by Wang et al. (2014) for two homologous three-ribbon flares that occurred in this active region more than a day later. These two flare arcades in the corona can be seen, for example, in the images made in the SDO/AIA "hot" 94 Å channel shown in Figure 2d and also in Figure 7 below.

Figure 2 also shows the location of the sources of X-ray emission reconstructed with the Clean algorithm (e.g. Hurford et al., 2002) using data of RHESSI's front Detectors 1, 3, 5 – 9. It can be seen that for a given 12-second time interval, the X-ray sources synthesized in two energy ranges of 6 – 12 and 12 – 25 keV had almost the same size and were located in the same place above the central flare ribbon and the negative polarity magnetic tongue. It is difficult to say unambiguously whether the X-ray sources were located exactly between the two loop systems or somewhere inside them because of observational limitations (limited

angular resolution and dynamic range of RHESSI, undefined inclination of the flare loops, projection effect). It can be noted that for all time intervals of the flare, a single X-ray source was observed, and the centroids in different energy ranges (< 25 keV) coincided within the limits of RHESSI's angular resolution. However, this source did not stand in one place – it systematically shifted from East to West during the flare (see Figure 7 and the analysis in Section 2.3).

2.2. Spectral Analysis of X-Ray Emission

We performed spectral analysis of the X-ray emission detected by RHESSI during the M1.1 flare using the *Object Spectral Analysis Executive* (OSPEX: Schwartz et al., 2002; Smith et al., 2002) within the *SolarSoft Ware* (SSW). This flare was not very powerful and did not show hard X-ray and γ-ray emission above ≈ 50 keV. For this reason, we implemented only four of the simplest and frequently used models to fit flare X-ray spectra: i) single thermal model (vth model) representing optically thin bremsstrahlung emission of plasma with Maxwellian velocity/energy distribution function, ii) double thermal model (2vth) representing bremsstrahlung emission of two populations of Maxwellian plasma with different temperatures and emission measure, iii) single thermal plus non-thermal thick target model (vth + thick2), and iv) single thermal plus non-thermal thin target model (vth + thin2). In models iii and iv it is assumed that in addition to the Maxwellian plasma population, there is also a single population of non-thermal (or accelerated) electrons with a decreasing power-law energy distribution. The bremsstrahlung of these non-thermal electrons is described in the approximation of thick and thin targets, respectively (see the review of different models by Holman et al., 2011).

There are three parameters in the vth model: emission measure of the plasma ($EM = \int n^2 dV$, where n and V are the emitting plasma density and volume, respectively), plasma temperature [T], and relative abundance for several elements to some standard coronal abundance (we kept this parameter fixed during the fitting procedure).

The 2vth model has five parameters: two plasma temperatures [T_1 and T_2], two plasma emission measures [EM_1 and EM_2], and the relative abundance (which, again, was kept fixed).

The vth + thick2 and vth + thin2 models have nine parameters each. The first three of them are the same as in the vth model. The fourth parameter in vth + thick2 is the total integrated electron flux [in 10^{35} electrons sec^{-1}] and in vth + thin2 is the normalization factor [in 10^{55} electrons cm^{-2} sec^{-1}], i.e. plasma density multiplied by source volume multiplied by integrated nonthermal-electron flux density. The fifth and seventh parameters in vth+thick2 are power-law indices [δ_1 and δ_2] of the electron flux distribution function, respectively, below and above the break energy E_{br}, which is the sixth parameter. For vth + thin2 these parameters are the same with the only difference being that they are for the electron flux density distribution function. The eighth and ninth parameters, in both vth + thick2 and vth + thin2, are the low [E_{lco}] and high [E_{hco}] energy cutoffs, respectively. We kept $E_{br} = 33$ MeV, $\delta_2 = 6$, and $E_{hco} = 32$ MeV fixed during the fitting procedure. In this way, i.e. by fixing $E_{br} > E_{hco}$ (which is a standard way in OSPEX), we have defined a population of non-thermal electrons without a break in a power-law spectrum defined by only one index [δ_1], which we will further denote δ for simplicity.

Examples of fitting the observed X-ray spectrum (in the energy range from 6 to 50 keV) by the four models for one 12-second time interval (indicated by two vertical dotted lines in Figure 1c,e) around the first flare peak are shown in Figure 3. It can be seen that all models except the first one (i.e., the vth model) can fit the spectrum reasonably well. We found the
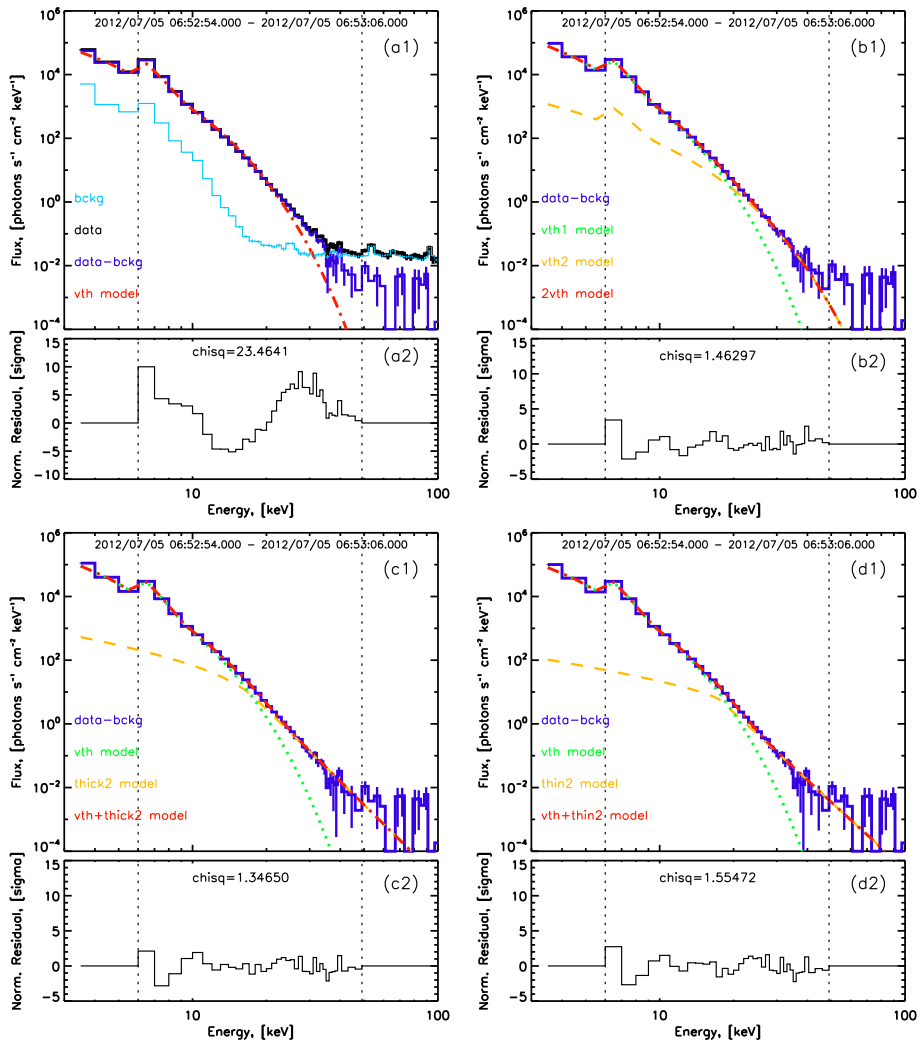
Figure 3 Example of the M1.1 flare X-ray spectrum fitting by four models: (**a**) single-temperature plasma bremsstrahlung model (vth), (**b**) two-temperature plasma bremsstrahlung model (2vth), (**c**) single-temperature plasma bremsstrahlung plus non-thermal thick target model (vth+thick2), (**d**) single-temperature plasma bremsstrahlung plus non-thermal thin target model (vth+thin2). The spectrum shown is for the 12-second temporal interval indicated by two vertical dotted lines in Figure 1c,e, and is the same one for which the X-ray sources are shown in Figure 2. The original spectrum ("data"), background spectrum ("bckg"), and background-subtracted spectrum ("data-bckg") are shown by *black*, *cyan*, and *blue color*, respectively, on (**a1**). We do not show "bckg" and "data" on (**b1**), (**c1**), and (**d2**) since they are almost the same as on (**a1**). The best-fit model spectrum is shown by the *red dash-dot curve*. The various components of the fit models are shown in different colors (and line types) and the designations are given on the panels with the corresponding colors. The normalized residual is shown in the *bottom panels* (**a2**, **b2**, **c2**, **d2**). The value of the normalized residual averaged over the energy interval considered (6–50 keV) is indicated as "chisq" in these *bottom panels*.
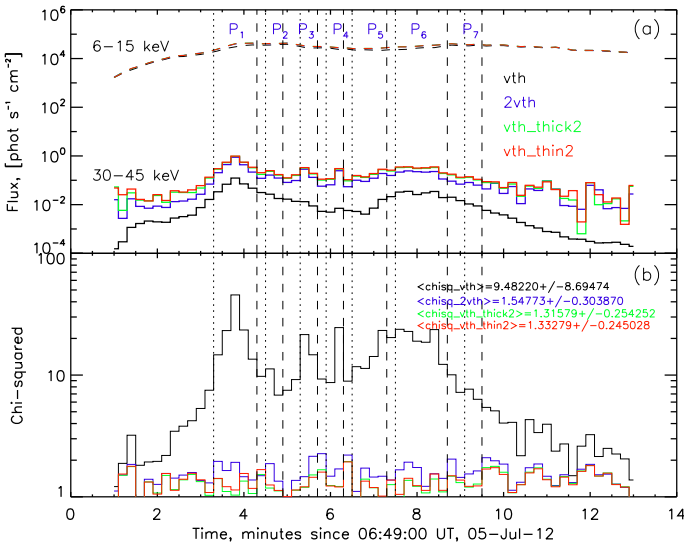
Figure 4 Quality of the M1.1 flare X-ray spectrum fit by four models: vth (*black*), 2vth (*blue*), vth+thick2 (*green*), vth+thin2 (*red*). (**a**) Model photon fluxes obtained by integrating the best-fit model X-ray spectra over two energy intervals: 6–15 keV (*dashed curves*) and 30–45 keV (*solid curves*). Note that the model photon fluxes in the 6–15 keV range (*dashed curves*) are almost the same for the four models and therefore overlap (see the text). (**b**) Normalized residuals averaged over the energy interval 6–50 keV selected for the fitting. The values averaged over the entire temporal interval of the flare are indicated on the panel by corresponding colors. The start and end of seven QPPs $P_1 – P_7$ (see Figure 5a) are shown by *vertical dotted and dashed lines*, respectively.

same situation for all time intervals during the flare. This is demonstrated in Figure 4b, where the temporal profiles of $\chi^2(t)$ are shown for the four models used. Its value for the vth model is always very high, and its average value is 9.5 ± 8.7, while for the 2vth, vth + thick2, and vth + thin2 it is 1.5 ± 0.3, 1.3 ± 0.3, and 1.3 ± 0.2, respectively, i.e. for these three models χ^2 is close to unity, and it is difficult to decide which spectral model is the most preferable. Figure 4b also shows the quasi-periodic variations of this coefficient for the vth model during the flare. This suggests that an additional population of very hot thermal plasma or nonthermal electrons, not described by the vth model, could appear and disappear quasi-periodically several times during the flare. This is manifested by similar small-amplitude quasi-periodic variations in the model X-ray fluxes in the 30–45 keV range, reconstructed from the fitted spectra by the 2vth, vth + thick2, and vth + thin2 models shown in Figure 4a. These model photon fluxes were obtained by integrating the best-fitted model spectra over the two indicated energy ranges of 6–15 and 30–45 keV for each 12-second time interval. We also note that the model photon fluxes in the 6–15 keV range (dashed curves in Figure 4a) almost coincide for the four considered models. This is because the X-ray spectrum in this range is almost completely determined by the bremsstrahlung spectrum of the "hot" plasma (i.e. the vth model), which is almost the same for all four models (see Figure 3).

2.2.1. X-Ray Spectra Fitting with the 2vth Model

These quasi-periodic variations are most clearly observed in the temporal profiles of the temperature and emission measure of the second population of Maxwellian plasma in the 2vth model (Figure 5). It can be seen from Figure 5a that kT_2 (where k is the Boltzmann constant)
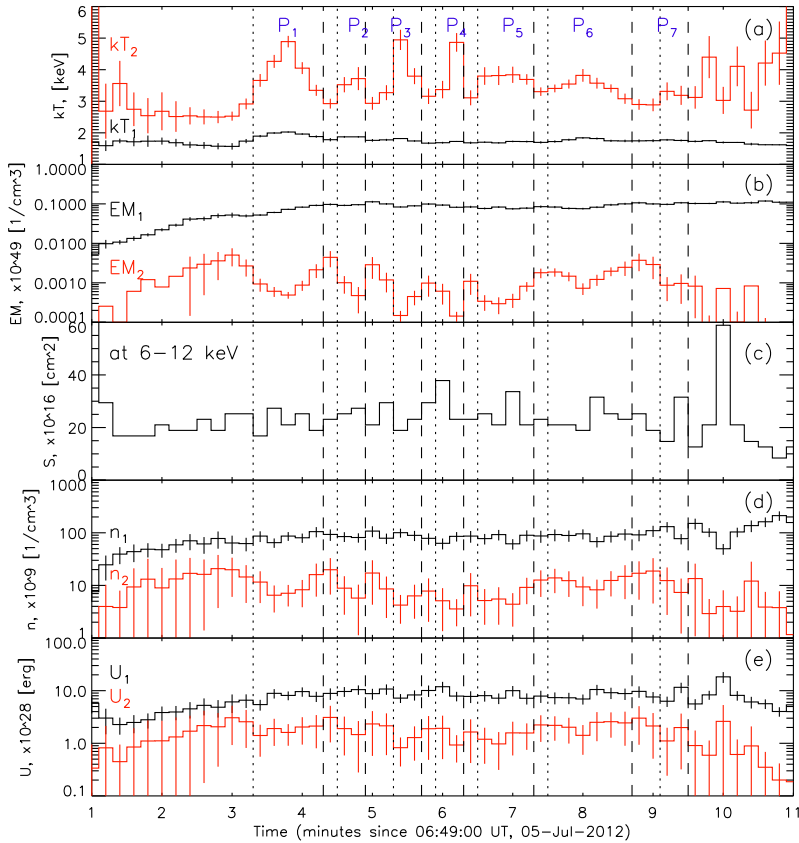
Figure 5 Temporal profiles of the physical parameters obtained from the M1.1 flare X-ray spectra best fit with the *2vth* model: (**a**) plasma temperature, (**b**) emission measure, (**c**) X-ray source visible area, (**d**) plasma density, (**e**) plasma thermal energy. Estimated errors of the parameters are shown by *vertical dashes*. Parameters for the hot and super-hot plasmas are shown by *black* and *red* colors and denoted by subscripts 1 and 2, respectively. The start and end of seven QPPs P_1 – P_7 in the super-hot plasma temperature profile on (**a**) are indicated by *vertical dotted and dashed lines*, respectively.

showed quasi-periodic variations in the range of values from ≈ 3 to ≈ 5 keV, corresponding to plasma temperature from ≈ 30 to ≈ 50 MK. Plasma with such a high temperature in solar flares is commonly referred to as "super-hot" plasma (e.g. Caspi, Krucker, and Lin, 2014; Sharykin, Struminskii, and Zimovets, 2015). One can see at least seven peaks (designated as P_1 – P_7) of varying amplitude and duration between $\approx 06 : 52$ UT and $\approx 06 : 59$ UT. The average time between adjacent peaks is $\langle P \rangle = 54 \pm 13$ seconds, i.e. the variations in duration are significantly less than the average duration. Such variations can be called quasi-periodic pulsations (QPPs). Obviously, in this case, we do not deal with some kind of stationary harmonic processes (or harmonic oscillations). Rather, we are probably dealing with a non-stationary process repeating at close intervals. It is interesting to note that the local maxima of T_2 correspond to the local minima of EM_2, i.e. they are in anti-phase. At the same time, the first (and the main, according to its much larger emission measure) plasma population with a temperature $T_1 \approx 16 - 20$ MK does not show such obvious high-amplitude quasi-periodic variations as the super-hot plasma. We will call this population "hot" plasma.

Figure 5c shows the temporal profile of the visible area [S] of the X-ray source (within the level of 50 % of the maximum) in the $6 - 12$ keV energy range reconstructed with the Pixon algorithm using the observational data of all nine RHESSI detectors. The integration time is 12 seconds, i.e. about three periods of RHESSI's rotation around its axis. As we already mentioned, there was a single X-ray source in any temporal interval during the considered part of the flare. The apparent source areas in two energy ranges of $6 - 12$ keV and $12 - 18$ keV were close to each other (see Figure 7 below), and due to this we suggest that both sources of the hot and super-hot plasmas had the same area determined as the area of the $6 - 12$ keV source (note that we could not reconstruct a sequence of high-quality images in higher-energy ranges during the entire flare due to low signal-to-noise ratio at higher energies). The apparent source area shows some variations that do not correlate with the QPPs of temperature and emission measure of the super-hot plasma. Using this source area (and suggesting that the plasma volume is related to the apparent area as $V \approx S^{3/2}$) and emission measure, we estimated densities of the hot and super-hot plasmas as $n_{1,2} \approx EM_{1,2}^{1/2} S^{-3/4}$. They are shown in Figure 5d, from which it can be found that the density of the hot plasma was around an order of magnitude higher than the density of the super-hot plasma. The estimations of the plasma temperature, density, and volume allow us to estimate the thermal (or internal) energy of the hot and super-hot plasmas as $U_{1,2} \approx 3n_{1,2}\mathrm{k}T_{1,2}f S^{3/2}$, the temporal profiles of which are shown in Figure 5e. For simplicity, we assumed that the volumetric filling factor $f = 1$ (e.g. Emslie et al., 2012). From Figure 5e, we can see that the thermal energy of the hot plasma exceeded the thermal energy of the super-hot plasma by about five times during all considered temporal intervals of the flare. Hence, it follows that the super-hot plasma could not be a source of heating for the hot plasma.

In Table 1 we summarized values of the various parameters of the hot and super-hot plasmas obtained in the framework of the 2vth model. In particular, one can see that the average value of the total thermal energy (of both hot and super-hot plasmas) in one pulsation $\langle\langle U_1 \rangle\rangle + \langle\langle U_2 \rangle\rangle = (12.2 \pm 2.0) \times 10^{28}$ erg, while the total thermal energy of all seven pulsations was $\Sigma U_1 + \Sigma U_2 = (85.7 \pm 12.0) \times 10^{28}$ erg.

In addition, we estimated the average energy loss by energetic electrons propagating through the source volume filled with the hot and super-hot plasmas as $El_{1,2} = \left(3K N_{1,2}\right)^{1/2} \approx 8.8N [19]_{1,2}^{1/2}$ keV, where $K = 2\pi e^4 \Lambda$, e is the electron charge, Λ is the Coulomb logarithm, $N [19]_{1,2} = N_{1,2}/10^{19}$ cm^{-2}, and the plasma column density is $N_{1,2} \approx n_{1,2}S^{1/2}$ (Brown, 1973; Veronig and Brown, 2004). We obtained the following average values: $El_1 = 19.2 \pm 0.8$ keV and $El_2 = 6.3 \pm 1.4$ keV. It is clear that energetic electrons lose more energy in the more dense hot plasma than in the less dense super-hot plasma with the same volume. This estimate tells us that all energetic electrons with energies $\lesssim 20$ keV could lose the major part of their energy quickly in the coronal source, contributing to the population of the hot plasma. In this case, the super-hot plasma with a characteristic particle energy of $\mathrm{k}T_2 \approx 3 - 5$ keV should quickly cool down to the characteristic energy of the hot plasma of $\mathrm{k}T_1 \approx 1.5 - 2$ keV. Since the super-hot plasma exists for approximately the duration of one pulsation $\langle P \rangle \approx 54 \pm 13$ seconds, it can be assumed that the super-hot plasma is located in a different region than the hot plasma. Since the X-ray sources of different energies were located in the image plane in almost the same place, it can be assumed that the super-hot plasma could be located above the volume of the hot plasma. Caspi and Lin (2010) showed by the analysis of RHESSI observations of one flare that the super-hot plasma source is indeed located above the hot plasma source in the corona. Examples of similar RHESSI observations of near-limb or partially beyond-limb events, when the coronal sources of higher-energy X-rays (and hence a more energetic population of particles) were located above the sources of less-energetic X-rays, were presented by, e.g., Sui and

Table 1 Physical parameters of the hot and super-hot plasmas obtained from the application of the 2vth model to the X-ray spectra of the M1.1 flare studied. $\langle \cdots \rangle$ means averaging over the main part of the flare from 06:52 to 06:59 UT, $\langle\langle \cdots \rangle\rangle$ – averaging over the QPPs $P_1 - P_7$, and Σ means summation over all QPPs. The thermal energy of each pulsation is defined as the peak thermal energy during its duration. Parameter designations are explained in the text.

Parameter	Value	Error	Units
$\langle EM_1 \rangle$	0.088	0.014	10^{49} cm^{-3}
$\langle EM_2 \rangle$	0.0013	0.0012	10^{49} cm^{-3}
$\langle EM_1/EM_2 \rangle$	67.4	62.8	–
$\langle kT_1 \rangle$	1.8	0.1	keV
$\langle kT_2 \rangle$	3.6	0.6	keV
$\langle T_1/T_2 \rangle$	0.5	0.1	–
$\langle S \rangle$	24.1	5.1	10^{16} cm^2
$\langle n_1 \rangle$	87.6	19.9	10^9 cm^{-3}
$\langle n_2 \rangle$	10.2	6.4	10^9 cm^{-3}
$\langle n_1/n_2 \rangle$	10.4	7.0	–
$\langle El_1 \rangle$	19.2	0.8	keV
$\langle El_2 \rangle$	6.3	1.4	keV
$\langle\langle U_1 \rangle\rangle$	10.3	1.6	10^{28} erg
$\langle\langle U_2 \rangle\rangle$	1.9	1.2	10^{28} erg
$\langle\langle U_1 \rangle\rangle + \langle\langle U_2 \rangle\rangle$	12.2	2.0	10^{28} erg
$\langle\langle U_1/U_2 \rangle\rangle$	5.4	3.5	–
ΣU_1	72.3	9.3	10^{28} erg
ΣU_2	13.4	7.6	10^{28} erg
$\Sigma U_1 + \Sigma U_2$	85.7	12.0	10^{28} erg
$\Sigma U_1/\Sigma U_2$	5.4	3.1	–

Holman (2003) and Liu et al. (2008). It was argued in these works that such an arrangement of X-ray sources is explained by reconnection in a quasi-vertical current sheet in the corona, with a more energetic plasma located closer to the center of the reconnecting current sheet.

The presence of accelerated electrons with a nonthermal energy spectrum is not assumed within the framework of the 2vth model. It is, however, assumed within the framework of the vth + thick2 and vth + thin2 models, which are considered in the following Section 2.2.2.

2.2.2. X-Ray Spectra Fitting with the vth + thick2 and vth + thin2 Models

Now let us consider together results obtained within the vth + thick2 and vth + thin2 models. The temporal profiles of different physical parameters obtained with both models are shown in Figure 6, and all of the main parameters (averaged or summed over all QPPs) are summarized in Table 2.

The fit quality within these two models is almost equal (see above), and the temporal evolution of the parameters is also very similar. The similar QPPs (although with some minor differences) can be seen in the temporal profiles of the total energy-integrated nonthermal electron flux for the vth + thick2 model and in the profile of the normalization factor N_f (i.e. plasma density multiplied by source volume multiplied by integrated nonthermal electron flux density) for the vth + thin2 model (Figure 6a). These profiles anticorrelate with the profiles of nonthermal electron spectral index [δ] (Figure 6b). This shows the well known
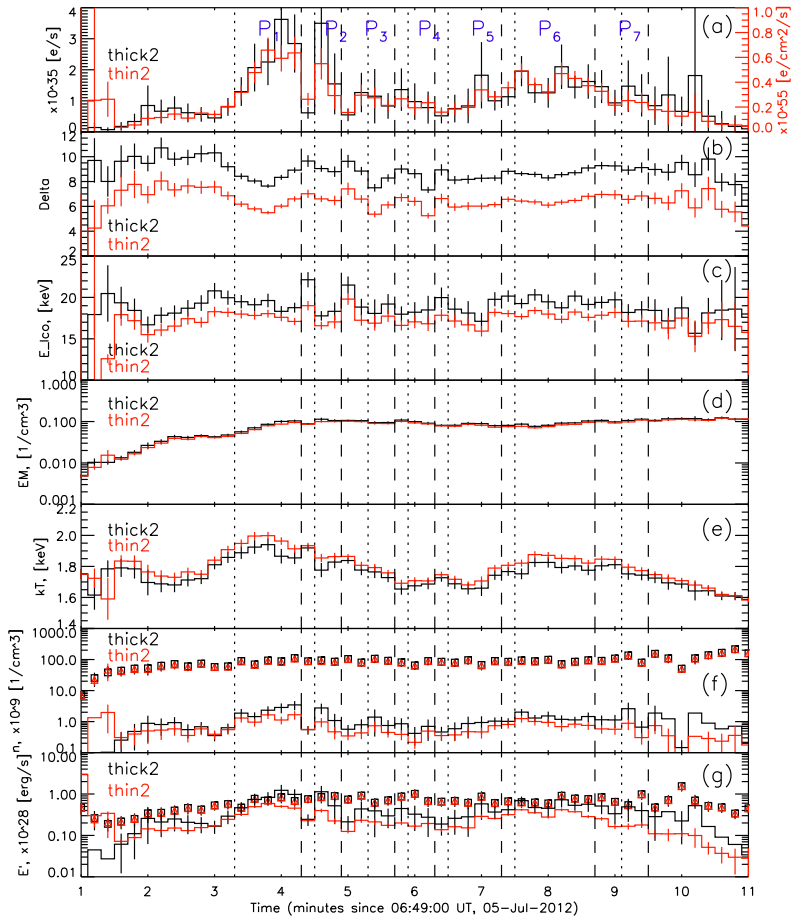
Figure 6 Temporal profiles of the physical parameters obtained from the M1.1 flare X-ray spectra best fit with the vth+thick2 (*black*) and vth+thin2 (*red*) models: (**a**) total integrated flux of non-thermal electrons (for vth+thick2) and normalization factor, i.e., plasma density multiplied by X-ray source volume and by integrated non-thermal electron-flux density (for vth+thin2), (**b**) absolute value of the power-law spectral index of electron flux (for vth+thick2) and electron-flux density (vth+thin2), (**c**) low-energy cutoff in the non-thermal electron distribution function, (**d**) emission measure of thermal plasma, (**e**) the temperature of thermal plasma, (**f**) the density of thermal plasma (*squares and triangles*) and non-thermal electrons (*solid curves*), (**g**) the energy of thermal plasma (*squares and triangles*) and non-thermal electrons (*solid curves*) per unit of time. Estimated errors of the parameters are shown by *vertical dashes*. The start and end of seven quasi-periodic pulsations $P_1 - P_7$ in the super-hot plasma temperature profile in the 2vth model (see Figure 5a) are indicated by *vertical dotted and dashed lines*, respectively.

"soft-hard-soft" spectral behavior and may indicate that the observed QPPs are the signature of successive episodes of electron acceleration in the flare region (see, e.g., the review by Holman et al., 2011). To note, the nonthermal electron spectra are very soft: $\delta = 8.6 \pm 0.6$ within the vth + thick2 model (for electron flux) and $\delta = 6.4 \pm 0.6$ within the vth + thin2 model (for electron flux density).

As in the 2vth model, the hot thermal plasma population (with $T \approx 16 - 20$ MK) did not show such QPPs in the profiles of emission measure (Figure 6d) and temperature (Figure 6e).

Table 2 Physical parameters of the hot thermal plasma and nonthermal electrons obtained from the application of the vth + thick2 and vth + thin2 models to the X-ray spectra of the M1.1 flare studied. $\langle \cdots \rangle$ means averaging over the main part of the flare from 06:52 to 06:59 UT, $\langle\langle \cdots \rangle\rangle$ – averaging over the QPPs $P_1 - P_7$, and Σ means summation over the QPPs. The thermal energy of each pulsation is defined as the peak thermal energy during its duration. Parameter designations are explained in the text.

Parameter	Value		Error		Units
	vth+thick2	vth+thin2	vth+thick2	vth+thin2	
$\langle EM \rangle$	0.093	0.087	0.014	0.013	10^{49} cm^{-3}
$\langle kT \rangle$	1.8	1.8	0.1	0.1	keV
$\langle S \rangle$	24.1	24.1	5.1	5.1	10^{16} cm^2
$\langle N_f \rangle$	1.46	0.34	0.98	0.16	[a]
$\langle \delta \rangle$	8.6	6.4	0.6	0.6	–
$\langle E_{lco} \rangle$	19.1	17.6	1.4	1.0	keV
$\langle n \rangle$	90.4	87.1	24.1	19.1	10^9 cm^{-3}
$\langle n_{nth} \rangle$	1.30	0.74	0.90	0.44	10^9 cm^{-3}
$\langle n/n_{nth} \rangle$	68.4	118.4	0.9	0.4	–
$\langle El \rangle$	19.5	19.1	0.8	0.8	keV
$\langle El_{nth} \rangle$	2.3	1.7	0.6	0.4	keV
$\langle\langle U \rangle\rangle$	10.7	10.5	1.3	1.2	10^{28} erg
$\langle\langle E_{nth} \rangle\rangle$	22.3	12.1	10.4	1.3	10^{28} erg
$\langle\langle U + E_{nth} \rangle\rangle$	33.0	22.6	10.5	1.8	10^{28} erg
$\langle\langle U/E_{nth} \rangle\rangle$	0.48	0.87	0.23	0.13	–
ΣU	74.7	73.6	9.0	7.8	10^{28} erg
ΣE_{nth}	156.1	84.8	65.2	7.8	10^{28} erg
$\Sigma U + \Sigma E_{nth}$	230.8	158.4	65.8	11.0	10^{28} erg
$\Sigma U/\Sigma E_{nth}$	0.48	0.87	0.21	0.12	–

[a]It is in $\times 10^{35}$ electrons sec^{-1} and $\times 10^{55}$ electrons cm^{-2} sec^{-1} for the vth+thick2 and vth+thin2 models, respectively.

We calculated densities of thermal plasma and nonthermal electrons (Figure 6f). It can be seen that vth + thick2 and vth + thin2 models give similar densities of nonthermal electrons $n_{nth} \approx 10^9$ cm^{-3}, which is about two orders of magnitude smaller than the density of hot thermal plasma $n \approx 10^{11}$ cm^{-3} (which, in its turn, is similar to the density of hot plasma obtained within the 2vth model). Using these values of densities, we estimated the energy losses by energetic electrons propagating through the hot plasma volume in the corona (as in Section 2.2.1) and found that it is $El \approx 18 - 20$ keV (for comparison, the energy losses by energetic electrons propagating through their own population with density $n_{nth} \approx 10^9$ cm^{-3} is only $El_{nth} \approx 1 - 3$ keV). It is interesting that the energy loss is very similar to the low cutoff energy of nonthermal electrons: $El_{nth} \approx E_{lco}$ (Figure 6c). This indicates that accelerated electrons with energies less than ≈ 20 keV could be efficiently thermalized in the coronal source and quickly leave the population of nonthermal electrons contributing to the population of hot thermal plasma.

We also calculated energy rates (i.e. total energy per second) of populations of hot plasma and nonthermal electrons (Figure 6g). These energy rates are comparable with each other, although nonthermal electrons contain slightly more (within a factor of two) energy during the QPPs. This can indicate the near equipartition of the released energy between thermal plasma and nonthermal electrons, or that the released energy first trans-

formed to the energy of nonthermal electrons, which were quickly thermalized and transformed their kinetic energy to the thermal energy of the hot plasma. The average total energy of thermal plasma and nonthermal electrons released during one pulsation was $\langle\langle U + E_{\mathrm{nth}}\rangle\rangle \approx (3.3 \pm 1.1) \times 10^{29}$ erg and $(2.3 \pm 0.2) \times 10^{29}$ erg for the vth + thick2 and vth + thin2 models, respectively. The total energy of thermal plasma and nonthermal electrons released during all QPPs within these two models was $\Sigma U + \Sigma E_{\mathrm{nth}} \approx (2.3 \pm 0.7) \times 10^{30}$ erg and $(1.6 \pm 0.1) \times 10^{30}$ erg, respectively.

It is interesting to note that the total kinetic energy of thermal plasma(s) and nonthermal electrons (both in the 2vth model and in the vth + thick2 and vth + thin2 models) released in one pulsation is in the range $\approx (1-4) \times 10^{29}$ erg. It corresponds to the energy of a microflare (e.g. Hannah et al., 2008a). Thus, the flare may be regarded as a sequence of microflare-like quasi-periodic episodes of energy release.

2.3. Analysis of X-Ray Source Dynamics

To restrict the number of possible mechanisms, it is important to know whether the quasi-periodic episodes of energy release happened in one place of the flare region (e.g. in one oscillating flare loop) or in different places, and if they happened successively in different places, then what are the dynamics of the energy-release site (e.g. Zimovets et al., 2021). This question is addressed in this subsection. We cannot observe the energy-release source (say, the reconnection site(s)) directly, but we can investigate apparent (i.e. in projection onto the photosphere) spatial evolution of the X-ray source during the flare.

To do this, we synthesized a series of images based on RHESSI's observational data in two energy ranges of $6-12$ keV and $12-18$ keV, in which there were high fluxes of X-ray photons above the background. We used three different algorithms – Clean, Pixon, and Forward Fit (e.g. Hurford et al., 2002; Dennis and Pernak, 2009) – which gave similar results.

Figure 7 shows positions of the flare X-ray source (synthesized with Clean) overlayed on the SDO/AIA images of the flare UV ribbons in the 1600 Å (left) and 1700 Å (middle) channels, and of the flare EUV sources in the 94 Å channel (right), integrated over the time intervals of seven successive QPPs (top row corresponds to P_1, bottom to P_7). One can see that: i) in each pulsation there was a single X-ray source with almost identical size and position in the $6-12$ and $12-18$ keV ranges, ii) this X-ray source was located above the central flare ribbon and systematically shifted predominantly from East (from pulsation P_1) to West (to pulsation P_7), iii) the flare EUV sources, resembling a double arcade of loops, also spread predominantly from East to West.

The systematic shifting of the centroid of the X-ray source ($6-12$ keV) in space during the flare is shown in Figure 8b. There, thin crosses show the position of the centroid (with uncertainties) for a sequence of temporal intervals of 12 seconds. This sequence of images was synthesized using the Forward Fit algorithm. The color of the crosses corresponds to the color in Figure 8a, which shows the X-ray emission-flux profile of the source. The seven bold crosses are the integrated positions of the source centroid (with a scatter) over the time of the seven QPPs. This figure clearly demonstrates the apparent systematic displacement of the X-ray source, from pulsation to pulsation, predominantly from East to West along the tongue of negative magnetic polarity.

A quantitative description of the kinematics of the X-ray source is presented in Figure 9. We calculated absolute values of the total "cumulative" (shown in the left column of Figure 9) and "instantaneous" (shown in the right column of Figure 9) displacements $[dr(t)]$ and velocities $[v(t)]$ of the X-ray source, and also along $[dr_{\mathrm{par}}(t), v_{\mathrm{par}}(t)]$ and perpendicular $[dr_{\mathrm{per}}(t), v_{\mathrm{per}}(t)]$ to a given direction, shown by the red dashed line in Figure
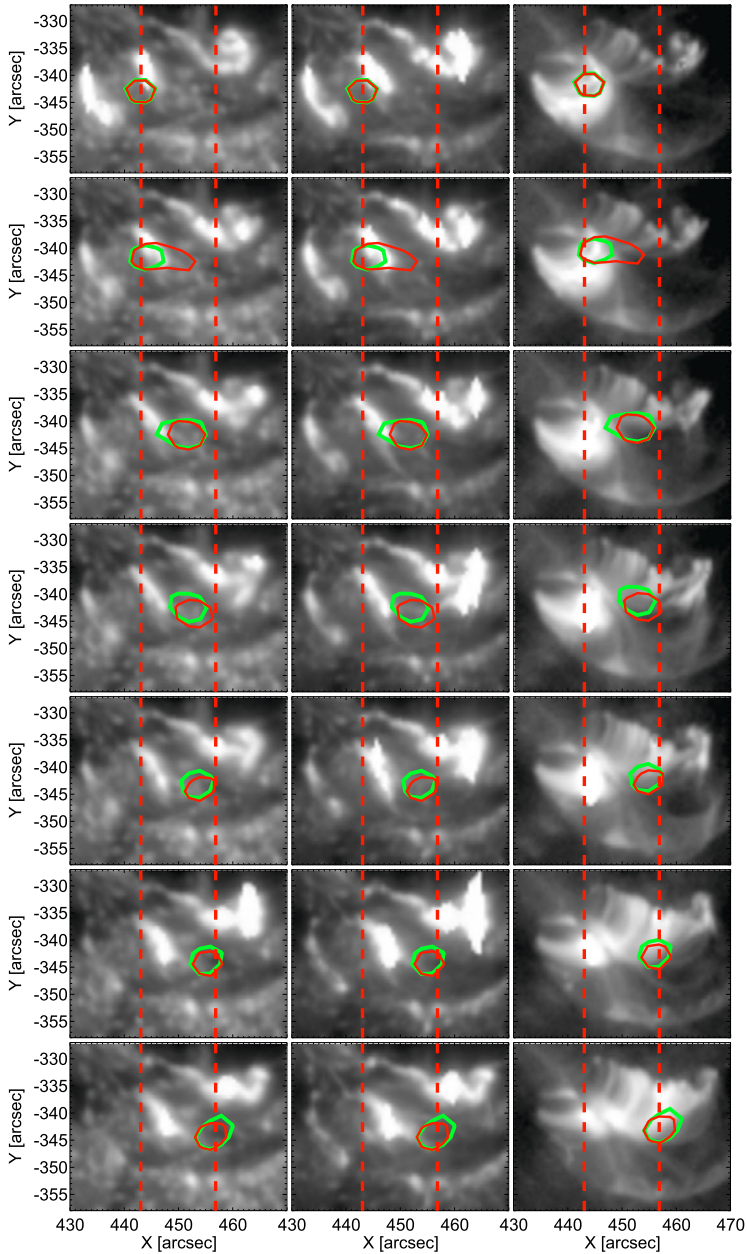
Figure 7 Evolution of the M1.1 flare X-ray, EUV, and UV sources during the seven QPPs $P_1 - P_7$ shown in Figure 5. *The left*, *middle*, and *right columns* are the SDO/AIA 1700 Å, 1600 Å, and 94 Å images, respectively, made near the peak time of the QPPs (*the upper row* corresponds to the pulsation P_1, *the lower row* to P_7). The X-ray sources synthesized from the data of RHESSI's detectors 1, 3, 5–9 using the Clean algorithm for the temporal intervals of the QPPs in $6-12$ keV and $12-18$ keV ranges are shown with the *green* and *red iso-contours*, respectively, at the level of 80 % from the maximum. *The left* and *right red vertical dashed lines* show the range of the Helioprojective-Cartesian coordinate x within which the centroid of the $6-12$ keV X-ray source shifted from P_1 to P_7 (from left to right, i.e. from East to West).
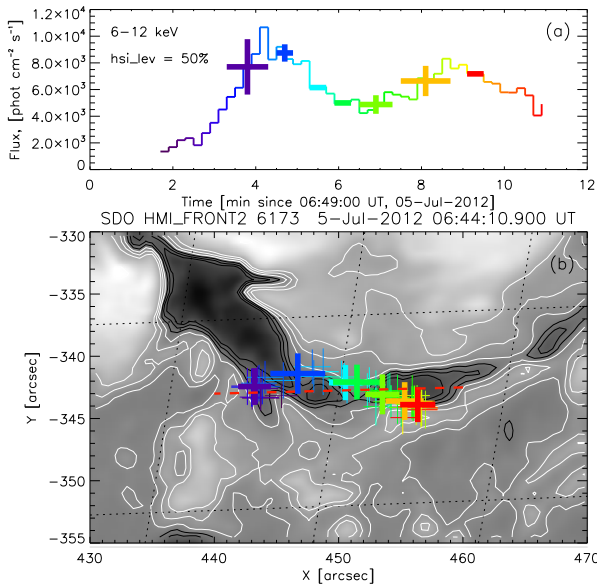
Figure 8 Dynamics and flux of the M1.1 flare X-ray ($6-12$ keV) source. (**a**) Temporal profile of the flux from the X-ray source area restricted by the iso-contour at 50 % from the maximum. The *color* (*from dark purple to red*) indicates the progression of time. *Thick horizontal* and *vertical bars* indicate the temporal intervals of QPPs $P_1 - P_7$ (see Figure 5) and the spread (one standard deviation) of the source flux within these time intervals, respectively. (**b**) *Thin crosses* show the position of the X-ray source centroid at successive temporal intervals of 12 seconds, *indicated by the corresponding color* in (**a**). Uncertainties in the centroid position in *x*- and *y*-directions are *indicated by horizontal and vertical segments*, respectively. The X-ray images were constructed for sequential temporal intervals of 12 seconds from observations of the RHESSI detectors $2-8$ using the Forward_Fit algorithm. *Thick crosses* show the centroid positions of X-ray sources (with uncertainties) averaged over the temporal intervals of successive pulsations $P_1 - P_7$ (*the color corresponds to the color of the crosses* in Panel **a**). The *background gray-scale image* is the map of B_{LOS} measured by SDO/HMI on the photosphere overlayed with iso-contours at levels $\pm100, \pm300, \pm500, \pm1500, \pm2500$ G (positive, i.e. towards the observer – *white*, negative – *black*). The *straight red dashed line* shows the general direction of the X-ray source motion along the tongue of negative magnetic polarity. The displacements and velocities of the X-ray source shown in Figure 9 are calculated relative to this direction. The projection of the 5°-step heliographic grid is shown as *thin black dotted arcs*.

8b, which is directed almost from East to West approximately along the tongue of negative magnetic polarity (or along a part of two PILs separating it from the regions of positive magnetic polarity on the South and North). The cumulative means $dr_{cum}(t_i) = r(t_i) - r(t_0)$ and $v_{cum}(t_i) = (r(t_i) - r(t_0))/(t_i - t_0)$, and the instantaneous means $dr_{inst}(t_i) = r(t_{i+1}) - r(t_i)$ and $v_{inst}(t_i) = (r(t_{i+1}) - r(t_i))/(t_{i+1} - t_i)$, where t_0 corresponds to the middle of the temporal interval of the first image of the sequence. We made these calculations for a sequence of images with a duration of 12 seconds each (the corresponding data points with uncertainties are shown with thin crosses), as well as for the positions of the sources integrated over the duration of each pulsation (shown with bold crosses).

From Figure 9 we can infer the following information:

i) before the start of the QPPs (before ≈06:52 UT), the X-ray source did not move systematically, and the position of its centroid varied only slightly;
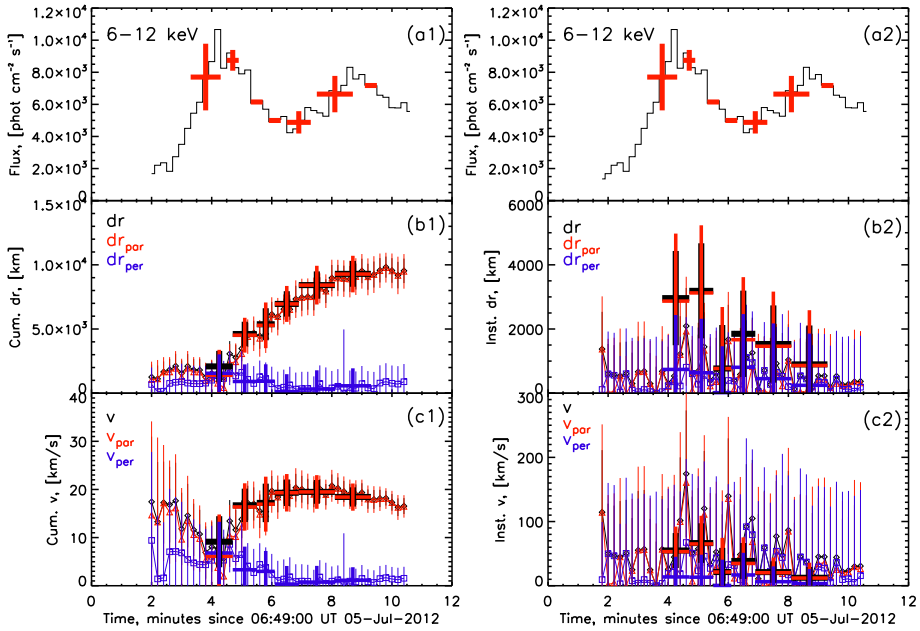
Figure 9 Flux and kinematics of the M1.1 flare X-ray ($6 - 12$ keV) source. (**a1**, **a2**) Temporal profile of the flux from the X-ray source area restricted by the iso-contour at 50 % from the maximum (*thin black histogram*). *Thick red horizontal and vertical bars* indicate the temporal intervals of QPPs $P_1 - P_7$ and the spread (one standard deviation) of the source flux within these time intervals, respectively. (**b1**) Cumulative (i.e. $|r(t_i) - r(t_0)|$) and (**b2**) instantaneous (i.e. $|r(t_{i+1}) - r(t_i)|$) displacements of the X-ray source centroid (with uncertainties). Total displacement – *black*, parallel and perpendicular displacements to the selected direction (shown by the *red dashed line* in Figure 8b) – *red* and *blue*, respectively. (**c1**) Cumulative and (**c2**) instantaneous velocities of the X-ray source centroid (with uncertainties), total – *black*, parallel and perpendicular to the selected direction – *red* and *blue*, respectively. *Thin lines* correspond to the X-ray source centroid found in the successive 12-second temporal intervals, *thick lines* – averaging over the temporal intervals of the QPPs $P_1 - P_7$ shown in Figure 5.

ii) the source began to systematically move mainly along the considered direction with the beginning of the appearance of the QPPs and almost stopped moving after their end ($\approx$06:58:30 UT);

iii) the source shifted along the given direction by ≈ 10 Mm in total during the QPPs, which is more than three times higher than the spatial resolution of the finest RHESSI collimator used (No. 2 ≈ 2.8 Mm);

iv) the distance between the average centroid position of successive pulsations was $dr_{par} \approx 1.8 \pm 1.0$ Mm;

v) the source moved at a low speed $v_{par} = 34 \pm 21$ km s^{-1} along a given direction, i.e. along the central flare ribbon above the negative magnetic tongue. The motion in the perpendicular direction was negligible, $v_{per} = 9 \pm 7$ km s^{-1}.

The values of the parameters of the instantaneous source motion, averaged over the pulsations, are summarized in Table 3.

Table 3 The parameters of the instantaneous motion of the $6-12$ keV X-ray source during the quasi-periodic pulsations P_1-P_7. $\langle\cdots\rangle$ means averaging over the pulsations. Parameter designations are explained in the text.

Parameter	Value	Uncertainty	Units
$\langle dr\rangle$	1867	1021	km
$\langle dr_{par}\rangle$	1793	997	km
$\langle dr_{per}\rangle$	483	306	km
$\max(dr)$	3190	–	km
$\max(dr_{par})$	3125	–	km
$\max(dr_{per})$	807	–	km
$\min(dr)$	769	–	km
$\min(dr_{par})$	769	–	km
$\min(dr_{per})$	17	–	km
$\langle v\rangle$	36	21	km s^{-1}
$\langle v_{par}\rangle$	34	21	km s^{-1}
$\langle v_{per}\rangle$	9	7	km s^{-1}
$\max(v)$	66	–	km s^{-1}
$\max(v_{par})$	65	–	km s^{-1}
$\max(v_{per})$	17	–	km s^{-1}
$\min(v)$	13	–	km s^{-1}
$\min(v_{par})$	12	–	km s^{-1}
$\min(v_{per})$	1	–	km s^{-1}

2.3.1. Comparison of Dynamics of X-Ray Sources in Homologous M1.1 and M6.1 Flares

It is interesting to compare the dynamics of X-ray sources in the investigated M1.1 flare with the dynamics of X-ray sources in the homologous M6.1 flare (SOL2012-07-05T11:39), which occurred in the same NOAA Active Region 11515 about five hours after the M1.1 flare. As we noted earlier, the general evolution of the soft X-ray temporal profiles of the M6.1 flare was very similar to the M1.1 flare. Like the M1.1 flare, the M6.1 flare was a three-ribbon flare. The flare ribbons and X-ray sources in both solar flares were located in approximately the same part of the Active Region 11515. This can be seen in Figure 10. From Figure 10, however, one can see a significant difference in the dynamics of X-ray sources of two flares: i) the X-ray sources during the M6.1 flare changed their position in space less systematically than in the M1.1 flare, ii) in contrast to the M1.1 flare, in some temporal intervals during the M6.1 flare, not one but two X-ray sources were observed – one between the southern and central flare ribbons (FR$_S$ and FR$_C$), the other between the central and northern ribbons (FR$_C$ and FR$_N$).

Similarly to how it was done for the M1.1 flare in Section 2.2, we fitted the X-ray spectra of the M6.1 flare using the same four models: vth, 2vth, vth + thick2, and vth + thin2. The results are presented in Figure 11. We can see from Figure 11b: first, that the vth and 2vth models did not fit the spectra well in the first half of the M6.1 flare, when there were significant fluxes of hard X-ray emission with energies above 50 keV. Second, we can see that the vth + thick2 and vth + thin2 models gave similarly good spectra fits throughout the entire M6.1 flare. Third, the most important for us, contrary to the M1.1 flare, there are no obvious quasi-periodic variations of the spectral-fit quality, as well as of the reconstructed fluxes of X-ray emission of the M6.1 flare, but rather irregular, chaotic variations are visible (Figure 11a,b).

Thus, we can conclude that, despite the general similarity of the two homologous M1.1 and M6.1 flares, a quasi-periodic process of energy release was found in the first of them,
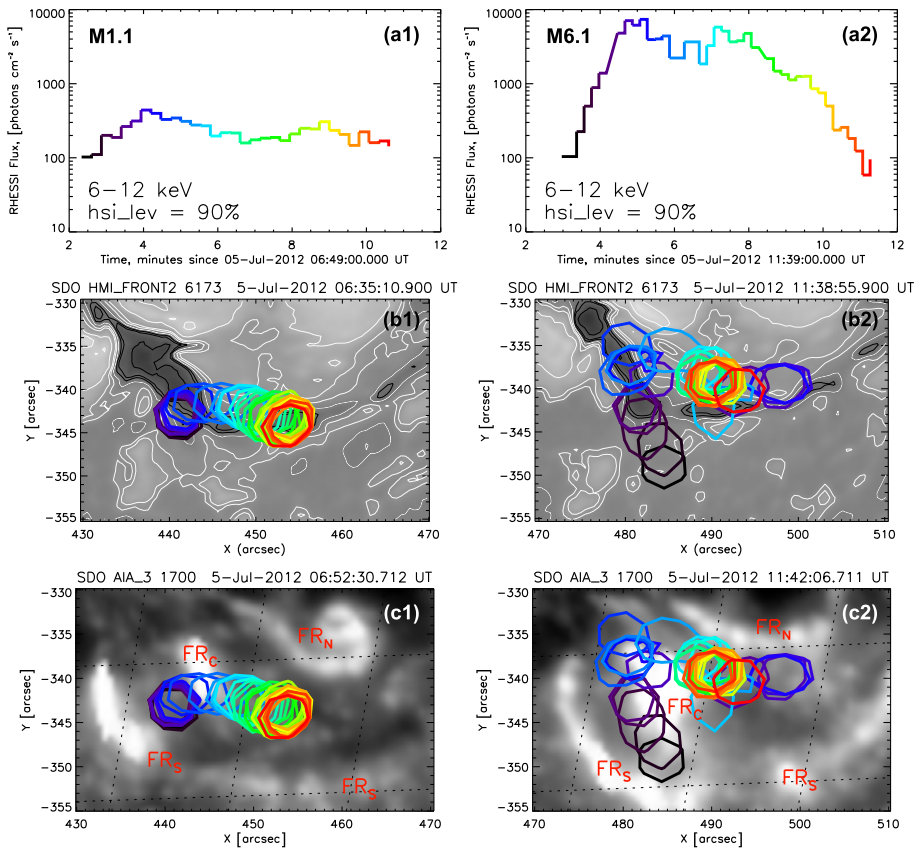
Figure 10 Comparison of dynamics of the 6 – 12 keV X-ray sources in two homologous three-ribbon flares M1.1 (*left*) and M6.1 (*right*). (**a1, a2**) Temporal profiles of the flux from the X-ray source area restricted by the iso-contour at 90 % from the maximum (shown in **b1, b2, c1, c2**). The color (from *black to red*) indicates the temporal progress. The X-ray images were constructed for sequential 12-second time intervals from observations of the RHESSI's detectors 2, 3, 5 – 9 using the Clean algorithm. (**b1, b2**) The *background gray-scale image* is the pre-flare map of B_{LOS} measured by SDO/HMI on the photosphere overlayed with *iso-contours* at levels 0, ± 100, ± 300, ± 500, ± 1000, ± 1500, ± 2000, ± 2500 G (positive, i.e. towards the observer – *white*, negative – *black*). (**c1, c2**) UV images of the flare region made in the SDO/AIA 1600 Å channel at some instant in the flare impulsive phase (*indicated above the image*). The south, center, and north flare ribbons are denoted as FR_S, FR_C, and FR_N, respectively.

accompanied by a systematic motion of the X-ray source, while in the second flare, a more chaotic dynamics of the sources was observed and there were no obvious quasi-periodic variations in fluxes and spectral parameters of X-ray radiation.

2.4. Extrapolation of Magnetic Field

To better visualize the 3D magnetic structure of the M1.1 flare region, we performed an extrapolation of the magnetic field from the photosphere to corona in the nonlinear force-free field (NLFFF) approximation. The 720-second pre-flare ($t_1 =$ 06:36:08 UT) and post-flare ($t_2 =$ 07:24:08 UT) vector magnetograms from SDO/HMI were used as the boundary conditions. The extrapolation was performed using the application of the optimization algo-
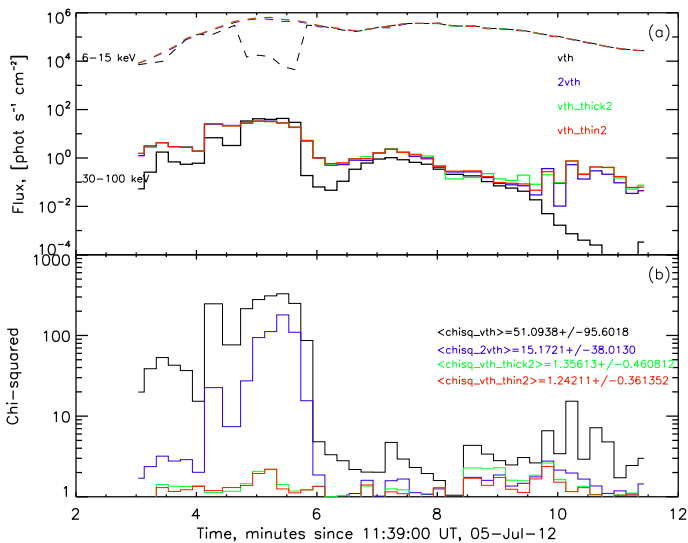
Figure 11   Check of the quality of the M6.1 (SOL2012-07-05T11:39) flare X-ray spectrum fit by four models: vth (*black*), 2vth (*blue*), vth+thick2 (*green*), vth+thin2 (*red*). (**a**) Model photon fluxes obtained by integrating the best-fitted model X-ray spectra over two energy intervals: $6-15$ keV (*dashed curves*) and $30-100$ keV (*solid curves*). Note that the model photon fluxes in the $6-15$ keV range (dashed curves) are almost the same for the four models (except vth in $\approx 11{:}43.5-11{:}46$ UT) and therefore overlap. (**b**) Normalized residuals averaged over the energy interval $6-100$ keV selected for the fitting. The values (with the standard deviations) averaged over the entire temporal interval of the flare are *indicated on the panel by corresponding colors*.

rithm (Wheatland, Sturrock, and Roumeliotis, 2000) developed by Rudenko and Myshyakov (2009). The same procedure and extrapolation parameters were used as by Sharykin et al. (2018) and Sharykin, Zimovets, and Myshyakov (2020). Note that the M1.1 flare studied was a confined event without a pronounced filament eruption (flux rope) or a coronal mass ejection (CME). There was a CME that started to be observed at 06:48:04 UT (i.e. before the onset of the M1.1 flare studied at 06:49 UT) in the SOHO/LASCO-C2 field-of-view, which was most probably associated with the previous $\approx$ C3.9 flare and eruption(s) that originated in the same active region more than half an hour ago earlier (see cdaw.gsfc.nasa.gov/CME_list/). Thus, the flare was probably not associated with very strong and dramatic magnetic reconfiguration of the active region, and we can rely upon the NLFFF approximation. We understand that a flare is inherently a dynamic phenomenon, and the magnetostatic approximation can be performed, with care, only before and after the flare. Indeed, the dynamics of the X-ray source investigated in the previous Section 2.3 clearly indicates the evolution of the magnetic configuration during the flare studied.

A comparison of some reconstructed magnetic-field lines with observations of the flare region in different wavelength ranges is shown in Figure 12. The field lines shown in Figure 12c,d (under two different viewing angles) were started from the supposed locations of the source of the X-ray pulsations $P_1 - P_7$ shown by the semi-transparent spheres. Their color corresponds to the color of the X-ray source of seven successive pulsations shown in Figure 8. The X- and Y-coordinates (i.e. longitude and latitude) of the centers of these spheres correspond to the X- and Y-coordinates of the pulsations' source centroids, while the Z-coordinate (above the photosphere) was suggested to be fixed at $Z_{sph} \approx 3.5$ Mm (i.e. ≈ 5 arcseconds), and the radius of these spheres is $R_{sph} = Z_{sph} \approx 3.5$ Mm. It is approximately equal to half the average distance between the neighboring flare ribbons and, thus,
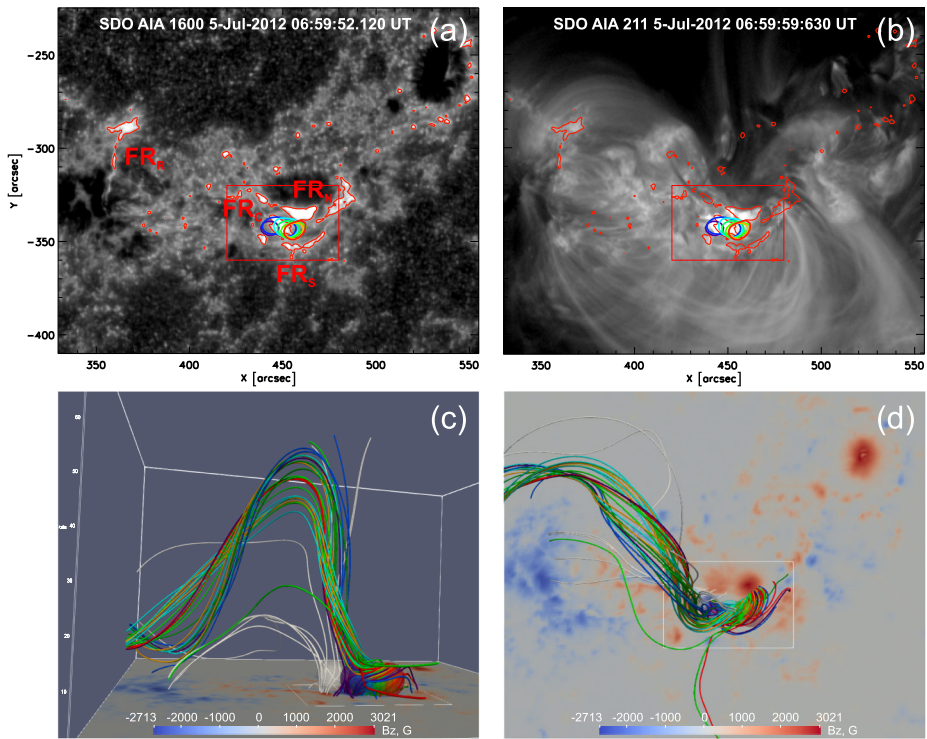
Figure 12 Comparison of observations of the M1.1 flare region (**a, b**) with the reconstructed magnetic-field lines started from the sites of the QPP sources (**c, d**). Images of the flare region made in the SDO/AIA 1600 Å (**a**) and 211 Å (**b**) channels at $\approx 07:00$ UT. *Red iso-contours* show the locations of the South (FR$_S$), central (FR$_C$), North (FR$_N$), and remote (FR$_R$) flare ribbons at the level of 1000 DN in the 1600 Å channel. Positions of the X-ray sources synthesized from the data of RHESSI's detectors 1, 3, 5 – 9 using the Clean algorithm for the temporal intervals of the QPPs P$_1$ – P$_7$ in the 6 – 12 keV energy range are shown with the iso-contours at the levels of 50 % from the maximum. *Their colors correspond to the colors of the QPPs* in Figure 8. Reconstructed magnetic-field lines started from the estimated positions of the QPP sources in the corona (shown by the semi-transparent spheres of the corresponding colors) are shown in (**c**) and (**d**) by the corresponding colors (from *dark blue* for the pulsation P$_1$ to *red* for P$_7$). (**c**) view from the side, (**d**) view from the top, the coordinates of the region shown approximately correspond to the HPC coordinates in (**a**) and (**b**). *Gray field lines* are started from the *gray semi-transparent sphere* and show a region of the magnetic "null-point" in the corona. *The background image on* (**c**) and (**d**) shows the B_z-component of the magnetic field on the photosphere. *The red and white rectangle on* (**a, b**) and (**c, d**), respectively, indicates the sub-region shown in Figure 2.

to the major radius of the loops connecting the neighboring ribbons, on the assumption that the loops are in the form of a round half-ring. Since the height of the X-ray sources is not known exactly, we visualized several field lines, the starting points of which in the corona for the calculation were randomly selected within the given spheres. Additionally, we added one more sphere (shown in gray) adjacent to the East of the dark purple sphere simulating the first pulsation P$_1$, in order to view the geometry of the magnetic field from the side from which the flare was developing (triggered). Closer views of the reconstructed field lines are shown in Figure 13a – c.

Figures 12 and 13 show the following: The sources of pulsations could be located in the western part of the quasi-horizontal leg of the large Ω-shaped system of twisted field
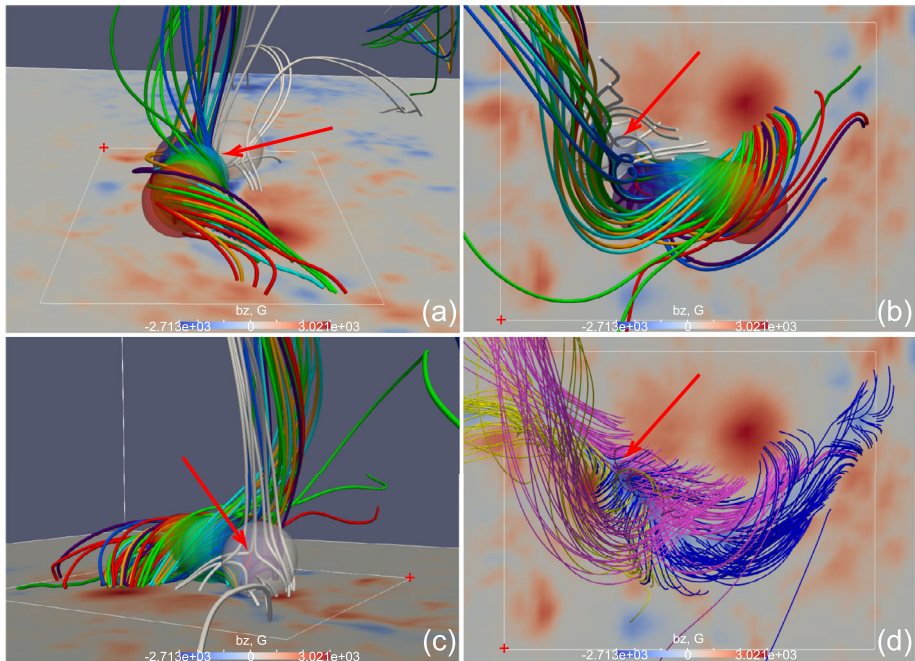
Figure 13 A closer (than in Figure 12c,d) view of the magnetic structure of the QPP producing region. (**a–c**) Reconstructed magnetic-field lines started from the estimated positions of the QPP sources in the corona (shown by the *semi-transparent spheres of the corresponding colors*) are shown by the corresponding colors (*from dark blue for the pulsation* P_1 *to red for* P_7). *Gray* field lines are started from the *gray semi-transparent sphere* and show a region of the magnetic "null-point" in the corona, which is indicated by the *red arrow*. (**d**) The same as in (**a–c**), except that: i) the locations of the X-ray sources are not shown, and ii) the magnetic-field lines are started from the regions of enhanced vertical electric currents on the photosphere, which are indicated in Figure 2 (*yellow* – the field lines from the south flare ribbon FR_S, *blue* – from the central ribbon FR_C, and *pink* – from the north ribbon FR_N). The background image shows the B_z-component of the magnetic field on the photosphere. The thin white rectangle indicates the sub-region shown in Figure 2. The *red cross* points to the same corner of the *white rectangle* on the photosphere as a reference point.

lines connecting the flare region with a region of the distant brightenings (or a remote flare ribbon, FR_R) far to the East (or somewhere nearby). This large loop system is visible in the SDO/AIA 211 Å image shown in Figure 12b. The twist of the west leg of this large loop system can be better seen in Figure 13a–c. The west footpoints of these twisted field lines are rooted in the regions of positive magnetic polarity in the vicinity of the south (FR_S) and north (FR_N) flare ribbons. The twisted field lines pass in the vicinity of two systems of loops (two magnetic arcades) with a large shear angle (almost up to 90° in the west part, i.e. almost parallel to the PILs) connecting the south (FR_S) and central (FR_C), north (FR_N) and central (FR_C) flare ribbons located in the regions of enhanced vertical electric currents on the photosphere (see Figures 2 and 13d).

An interesting feature is the presence of field lines in the eastern part of the flare region, forming something like a magnetic null-point in the corona (it is indicated by the red arrow in Figure 13). This "null-point" is located to the East of the source of the first pulsation P_1 and very close to it (a few Mm). We did not find a continuation of this null-point (or "null-line") to the West into the pulsation-producing region. As was noted above, there is a bundle of twisted field lines forming the west leg of the bundle of large coronal loops.

The magnetic field in the corona in the region of X-ray sources (at heights of $\approx 5 - 10$ Mm) was very inhomogeneous. It varied widely from $\min(B) \approx 150$ to $\max(B) \approx 750$ G (we use these values in Section 3 to estimate the range of possible Alfvén speed). The size of the coronal volume of the entire active region taken into consideration is $l_x \times l_y \times l_z \approx 199 \times 141 \times 85$ Mm and, thus, the volume is $V \approx 2.39 \times 10^{30}$ cm^3. We estimated the total magnetic energies of the nonlinear force-free and potential fields in the active region before ($E_{\mathrm{NLFFF},t_1} = \int \left(B_{\mathrm{NLFFF},t_1}^2 / 8\pi \right) dV \approx 2.35 \times 10^{33}$ erg and $E_{\mathrm{PF},t_1} = \int \left(B_{\mathrm{PF},t_1}^2 / 8\pi \right) dV \approx 1.61 \times 10^{33}$ erg) and after ($E_{\mathrm{NLFFF},t_2} \approx 2.36 \times 10^{33}$ erg and $E_{\mathrm{PF},t_2} \approx 1.64 \times 10^{33}$ erg) the flare. These values are slightly different for different boundaries of a 3D cube that bounds the region of interest. It can be seen that the total magnetic energies of both NLFF and potential fields are slightly higher after the flare than before it. Similar behavior was reported, e.g., by Schrijver et al. (2008). This could be due to the emergence of a new magnetic field from under the photosphere and its dynamics in the active region during the considered time interval. However, the ratio of the total magnetic energies of the NLFF and potential fields decreased during the flare (from $E_{\mathrm{NLFFF},t_1}/E_{\mathrm{PF},t_1} \approx 1.46$ to $E_{\mathrm{NLFFF},t_2}/E_{\mathrm{PF},t_2} \approx 1.44$), as well as the free magnetic energy decreased (as expected) by an amount $\Delta E_{\mathrm{free}} = E_{\mathrm{free},t_1} - E_{\mathrm{free},t_2} = \left(E_{\mathrm{NLFFF},t_1} - E_{\mathrm{PF},t_1} \right) - \left(E_{\mathrm{NLFFF},t_2} - E_{\mathrm{PF},t_2} \right) \approx 1.56 \times 10^{31}$ erg. This value of the released free magnetic energy is about an order of magnitude larger than the total energy of hot and super-hot plasmas or hot plasma and nonthermal electrons integrated over the duration of all QPPs estimated in the framework of the considered 2vth, vth + thick2, and vth + thin2 models. The excess of the released free magnetic energy could be spent, for example, on the acceleration of ions, electromagnetic radiation in the flare region, hydrodynamic plasma flows, various types of waves, etc. (e.g. Emslie et al., 2012).

3. Discussion

Let us first summarize the main results of the data analysis:

i) *The observed flare geometry.* The M1.1 flare had three main ribbons. The south (FR$_S$) and north (FR$_N$) ribbons were located in the regions of positive magnetic polarity, and the central ribbon (FR$_C$) was located in the magnetic tongue of negative polarity sandwiched between two regions of positive polarity on the South and North. The flare happened mainly in the central part of this negative magnetic tongue elongated from East to West by ≈ 15 Mm and from South to North by ≈ 5 Mm. The flare ribbons were located in the elongated regions of enhanced vertical electric currents. The south ribbon was located in the region of positive vertical current and the north ribbon in the negative vertical current, while the south/north parts of the central ribbon were mainly in the negative/positive vertical currents. Such a magnetic and electric-current topology corresponds to two adjacent magnetic arcades with a shear – the south one connecting the south and central ribbons and the north one connecting the central and north ribbons. These two arcades were visible, e.g. in the EUV images of the SDO/AIA hot 94 Å channel. The brightness in these two arcades (more in the north arcade) shifted from East to West during the flare. There was another remote brightening (or remote flare ribbon, FR$_R$) northeast (≈ 70 Mm) of the main three flare ribbons FR$_S$, FR$_C$, and FR$_N$. It was connected with the main flare region by the large system of coronal loops. In general, this magnetic topology resembles the topology determined by Wang et al.

(2014) for two other three-ribbon flares that occurred in the same NOAA Active Region 11515 more than a day after the flare that we are examining;

ii) *Flare X-ray spectra.* The spectra of the flare X-ray emission measured by RHESSI were fitted fairly well with three different models: 2vth, vth + thick2, and vth + thin2. It is difficult to make an unambiguous choice between these models relying only on the obtained values of the χ^2 parameter. Within the 2vth model, it was found that there were two populations of Maxwellian plasma – the hot plasma with a characteristic temperature $T_1 \approx 15 - 20$ MK and the super-hot plasma with $T_2 \approx 30 - 50$ MK. Temporal profiles of the temperature and emission measure of the super-hot plasma showed quasi-periodic variations with the average period $P \approx 54 \pm 13$ seconds between successive peaks. These variations were clearly not stationary harmonic oscillations, and for this reason we did not even try to estimate their significance using Fourier or wavelet analysis. We estimated various parameters of the hot and super-hot plasma populations (see Table 1) and found that the thermal energy of hot plasma exceeded the thermal energy of super-hot plasma by about five times; hence the energy of super-hot plasma was not enough to heat the hot plasma. The total thermal energy of hot and super-hot plasmas released in one pulsation was $\approx (1.2 \pm 0.2) \times 10^{29}$ erg, which corresponds to the energy of a microflare. The vth + thick2 and vth + thin2 models gave similar results. The temporal profiles of nonthermal electron fluxes and power-law spectral index [δ] showed similar quasi-periodic, non-harmonic variations, and the known soft-hard-soft spectral behavior was found. The spectra of nonthermal electrons were very soft, e.g. $\delta = 8.6 \pm 0.6$ within the vth + thick2 model (Table 2). The energy of nonthermal electrons was around twice higher than the thermal energy of hot plasma, and hence nonthermal electrons could heat the hot plasma. The total energy of nonthermal electrons and hot plasma in one pulsation was $\approx (2-4) \times 10^{29}$ erg, which also corresponds to the energy of a microflare;

iii) *Dynamics of the flare X-ray sources.* RHESSI observations showed a single X-ray source located above the central flare ribbon. The centroids of this source in different energy ranges ($6 - 12$, $12 - 18$, and $18 - 25$ keV) coincided within the RHESSI's angular resolution. An interesting feature is that the X-ray source was systematically displaced along the central flare ribbon and negative magnetic tongue from East to West with the slow speed $v_{par} = 34 \pm 21$ km s^{-1} during the observation period of the quasi-periodic energy release. The average distance between the source centroids of two successive pulsations were $dr_{par} = 1.8 \pm 1.0$ Mm. It is noteworthy that in the homologous three-ribbon M6.1 flare, the apparent motion of X-ray sources was less systematic and less ordered than in the M1.1 flare, and in the M6.1 flare there were no noticeable quasi-periodic variations in the temporal profiles of the spectral fitting parameters. Hence, we assume that the quasi-periodicity of the energy release in the M1.1 flare could be associated with the systematicity of the X-ray source motion;

iv) *NLFFF reconstruction.* The result of magnetic-field extrapolation from the photosphere to the corona is, in general, consistent with the observed flare geometry. The extrapolated field lines could reproduce two systems of highly sheared loops (two sheared arcades) connected the nearby flare ribbons $FR_S - FR_C$ and $FR_C - FR_N$, and also the large loop system connected the main flare region with the remote brightening region, FR_R, on the East. The field lines, which form this large loop system, have an Ω-like shape. Its east foot corresponds to FR_R, and its west leg is curved and twisted and corresponds to positions of the sources of X-ray pulsations. We also found that some extrapolated field lines form a null-point-like region in the corona slightly (a few Mm) East of the first pulsation's source. It can be assumed that the initial energy release of the flare was initiated in the vicinity of this null-point and then spread from East to West, which was

observed in the form of a moving source of pulsations. The drop in the free magnetic energy of the active region during the flare was $\approx 1.56 \times 10^{31}$ erg, which is about an order of magnitude higher than the total energy of hot plasma and super-hot plasma (or nonthermal electrons) released during all pulsations. This agrees with the general concept that solar flares are powered by free magnetic energy (e.g. Priest and Forbes, 2002; Emslie et al., 2012) and additionally indicates the adequacy of the NLFFF extrapolation performed.

The geometry and evolution of this M1.1 three-ribbon flare are clear to some extent. It can be roughly interpreted within the framework of the scenario proposed by Wang et al. (2014) for two other homologous three-ribbon flares observed in the same active region on the next day. The main concept of that work is that a null-line is present in the corona above the central flare ribbon, around which a current sheet (with the guide field) is formed, and a three-dimensional magnetic reconnection in this coronal current sheet during the flares heats plasmas and/or accelerates electrons, which go down along the magnetic-field lines – along the loops of two sheared arcades – into the chromosphere, as a result of which the plasma heats up there and three main flare ribbons become visible. The remote flare brightening in the chromosphere is associated with the transfer of released energy from the reconnecting current sheet along the long, curved spine field lines closed to the photosphere there (see the illustration in Figure 5 of Wang et al., 2014). On the other hand, we did not find a null-line in the region of the sources of pulsations, but we did find there a curved and twisted system of magnetic-field lines. Alternatively, these curved field lines could experience an upward magnetic-tension force and could begin to rise after a triggering disturbance in the vicinity of the null-point. This could lead to the formation of a current sheet in the corona and magnetic reconnection there (see Subsection 3.2.2 below). This is more reminiscent of the scenario discussed by Grechnev et al. (2020) in the context of analyzing two three-ribbon flares that happened in another active region.

3.1. Super-Hot Plasma vs. Nonthermal Electrons

One important question that remains unclear is: *whether there was an acceleration of nonthermal electrons with power-law energy spectra or heating of plasma to the super-hot temperatures during this quasi-periodic flare-energy release*. As was shown, the analysis of X-ray spectra of this flare does not unambiguously answer this question. Estimations of the energetics of thermal (Maxwellian) plasmas, nonthermal electrons, and magnetic field also did not help to answer this question.

One more possibility is to check for the presence of beams of energetic electrons in the corona during the pulsations by checking for the presence of the Type-III radio bursts. It is known that many solar flares of different GOES classes, including B and C classes, and even microflares, which are accompanied by acceleration of nonthermal electrons observed in hard X-rays, are also accompanied by Type-III radio bursts (e.g. Aschwanden et al., 1995; Hannah et al., 2008b; Reid and Ratcliffe, 2014). It was also found that QPPs of hard X-ray and microwave emissions are also accompanied, at least in some flares, by quasi-periodic Type-III bursts (Kumar, Nakariakov, and Cho, 2016; Kupriyanova et al., 2016; Li et al., 2020; Clarke et al., 2021). For this, energetic electrons need to have access to "open" field lines or large-scale coronal loops. The NLFFF extrapolation showed that there could be such field lines near the sources of pulsations (and the coronal null-point) in the flare studied (Figure 12). However, the dynamic radio spectrograms made with different radio spectrometers within the e-Callisto network (Benz et al., 2009, www.e-callisto.org/) do not show any radio bursts in the broad frequency range $\approx 8 - 1450$ MHz (Figure 14c – e), where the coronal and

interplanetary Type-III radio bursts are usually observed (e.g. Reid and Ratcliffe, 2014). One might assume that fluxes of energetic electrons were too small to generate a meaningful radio signal. However, against this suggestion, it can be pointed out that even in the microflare in which Hannah et al. (2008b) detected Type-III radio bursts, the power and total energy in energetic electrons, determined from the RHESSI spectral analysis of hard X-rays, were less than the power and total energy of nonthermal electrons in each pulsation in the M1.1 flare we are studying.

Another argument that is not in favor of accelerated electrons is the suspiciously high values of nonthermal electron spectral index ($\delta = 8.6 \pm 0.6$). However, this is also not a very strict argument since similarly large values of the electron spectral index were found in other flares and microflares (e.g. Hannah et al., 2011; Sharykin et al., 2016).

Microwave fluxes were low during the flare (Figure 14b). The peak flux at a frequency of 8.8 GHz measured at the Learmonth station of the *Radio Solar Telescope Network* (RSTN) in the vicinity of the time of the fourth pulsation P_4 was about 60 SFU. QPPs in the microwave range were not visible. Only individual weak peaks at 8.8 and 15.4 GHz could be seen in the vicinity of the times of pulsations P_1, P_4, and P_5 (Figure 14a,b). Preliminary spectral analysis showed that microwave spectra can be described in terms of both gyrosynchrotron radiation of the hot and super-hot plasmas and the hot plasma and nonthermal electrons with a power-law distribution (this analysis will be presented in a separate work). In summary, we cannot unambiguously answer the question stated at the beginning of this paragraph.

3.2. Possible Mechanisms of Quasi-Periodic Energy Release

Further, we concentrate on discussion of the following important question: *which of the known mechanisms of QPPs is better suited for the interpretation of the quasi-periodic character of energy release in the considered M1.1 three-ribbon flare.*

A recent comprehensive review of the QPPs' mechanisms in flares is presented by Zimovets et al. (2021). It is discussed there that many mechanisms can have similar observational manifestations in flares. However, different mechanisms can also have different specific observational features. The more observational features satisfy the mechanism's predictions, the more likely this mechanism could play a role in a particular flare.

Let us list the main observational properties of the QPPs in the investigated three-ribbon flare: i) the pulsations were definitely not stable harmonic oscillations, rather they represented a sequence of bursts with similar durations ($P_{QPP} = 54 \pm 13$ seconds) between successive peaks, ii) the pulsations represented a series of successive episodes of energy release, manifested in quasi-periodic formation and disappearance of populations of super-hot thermal plasma or nonthermal electrons, iii) definitely, these episodes of energy release happened in different places of the flare regions, rather than in one place (e.g. in one flare loop), because the systematic displacement of the X-ray source was clearly observed during the flare, iv) it is of special importance that the source motion was along a certain direction – along (and above) the central flare ribbon situated between two PILs on the South and North, i.e. along the adjacent sides of two flare arcades, and the speed of this apparent motion was very small (less than 65 km s^{-1} maximum), much less than the typical sound ($v_s \approx 152 T^{1/2}$ [MK] km s^{-1}) and Alfvén ($v_A \approx 2.18 \times 10^6 B$[G]$n^{-1/2}$ [cm^{-3}] km s^{-1}) speeds in the flare region in the solar corona. We do not know precisely the physical conditions in the flare region. Under a very broad range of possible plasma temperatures from the normal coronal temperature $T_c \approx 1$ MK to the maximal estimated super-hot plasma's temperature max $(T_2) \approx 50$ MK, we get $150 \lesssim v_s \lesssim 1100$ km s^{-1}. To estimate the range of
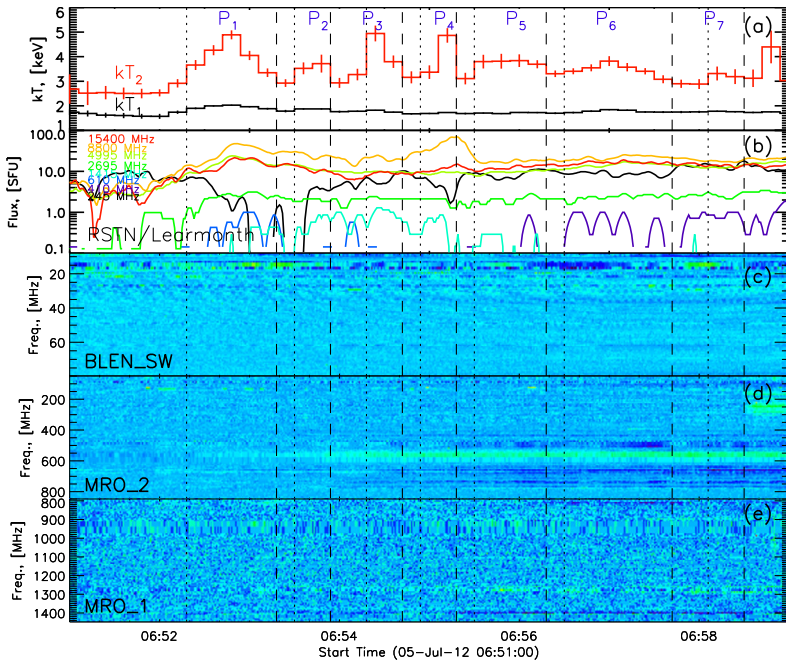
Figure 14 Check for the presence of QPPs in solar radio data. (**a**) Temporal profiles of the temperature of the hot (*black*) and super-hot (*red*) plasmas obtained within the 2*v*th model. (**b**) Temporal profiles of the background-subtracted flux density of solar radio emission detected at eight frequencies (from 245 MHz to 15.4 GHz) at the Learmonth station of the *Radio Solar Telescope Network* (RSTN). Background-subtracted spectrograms of solar radio emission in three frequency ranges: $8.0 - 79.625$ MHz (**c**), $49.988 - 846.238$ MHz (**d**), and $789.988 - 1445.550$ MHz (**e**) obtained by the instruments at the Bleien Observatory (BLENSW) and Metsähovi Observatory (MRO_2 and MRO_1), respectively. The start and end of seven quasi-periodic pulsations $P_1 - P_7$ in the super-hot plasma temperature profile in the 2*v*th model are indicated by the *vertical dotted and dashed lines*, respectively.

possible Alfvèn speed, we use $\min{(n)} = \min{(n_2)} \approx 4 \times 10^9$ cm^{-3}, $\max{(n)} = \max{(n_1)} \approx 1.2 \times 10^{11}$ cm^{-3} (see Tables 1, 2), $\min{(B)} \approx 150$ G, and $\max{(B)} \approx 750$ G (see Section 2.4), and we get $940 \lesssim v_A \lesssim 2.6 \times 10^4$ km s^{-1}.

Taken together these observational properties help to exclude many QPP mechanisms from consideration, in particular, all mechanisms related to direct emission modulation by MHD and electrodynamic oscillations of all types (group 1 mechanisms according to Kupriyanova et al., 2020). After discarding the mechanisms that do not satisfy the observations, the following are left:

i) autowave processes, in particular the mechanism based on slow magnetoacoustic waves acting as a reconnection trigger (Nakariakov and Zimovets, 2011);

ii) zipping or whipping reconnection associated with uneven reconnection in a current sheet during an asymmetric rise (eruption) of a twisted magnetic flux rope;

iii) flapping oscillations of a quasi-vertical current sheet in the corona (Artemyev and Zimovets, 2012);

iv) mechanism based on the thermal instability of a current sheet (Ledentsov and Somov, 2016).

Let us discuss the possibility of applying these mechanisms to the considered flare in a little more detail. This, of course, does not mean that any of these mechanisms should have necessarily worked in the considered flare region. It is possible that some other mechanism was actually at work, which we do not know about.

3.2.1. Slow Magnetoacoustic Waves as a Possible Trigger

This mechanism was proposed by Nakariakov and Zimovets (2011) to interpret QPPs in two-ribbon flares where the trigger of energy release systematically propagates along the PIL with a low speed less than v_s or v_A. Such low speeds are characteristic of the motions of flare sources along the PIL observed in different spectral ranges: in hard X-rays (e.g. Bogachev et al., 2005; Grigis and Benz, 2005; Kuznetsov et al., 2016), soft X-rays (e.g. Vorpahl, 1976; Aulanier et al., 2007), UV/EUV (Qiu et al., 2017), and microwaves (e.g. Kim et al., 2013; Kuznetsov et al., 2017). The plausibility of the interpretation of the observed evolution of two-ribbon flares in terms of slow magnetoacoustic waves in magnetic arcades was demonstrated by Gruszecki and Nakariakov (2011) via 2D numerical MHD simulation.

Following the standard model of two-ribbon flares, this mechanism assumes the presence of an X-line and/or a current sheet at the apex of the magnetic arcade. A packet of slow magnetoacoustic waves is excited in the region of primary energy release (perturbation) in the corona and propagates at a small angle to the magnetic field. For a wide range of ratios of the sound and Alfvén speeds, the maximum group velocity of waves perpendicular to the magnetic field corresponds to propagation at an angle $\alpha \approx 25° - 28°$ to the field. At the foot of the arcade, due to a strong density gradient, part of the waves is reflected back and propagates upward at a slight angle to the field until it reaches the X-line. There, the waves initiate locally an episode of magnetic reconnection, which heats the plasma and accelerates particles that cause electromagnetic radiation. Due to the plasma-pressure perturbations, a new packet of slow magnetoacoustic waves is generated, which propagates further along the arcade at a slight angle to the field, and the process is repeated, but in a different part of the arcade. Thus, a slow progression of the energy-release region and emission sources along the arcade and the PIL is observed.

We assume that this mechanism, in principle, could be adapted to the scenario of the three-ribbon flare proposed by Wang et al. (2014). As there, we also assume the presence of a null-line and/or a current sheet at the top between the two arcades. A two-dimensional projection of the simplified three-dimensional geometry of the model flare region onto the photosphere (i.e. top view) is shown in Figure 15. Three cases are shown: i) $\gamma = 0$, ii) $0 < \gamma < \pi/2$ and $\alpha + \gamma < \pi/2$, and iii) $0 < \gamma < \pi/2$ and $\alpha + \gamma > \pi/2$. We recall that originally the mechanism was considered for the magnetic shear angle $\gamma = 0$ (see Nakariakov and Zimovets, 2011). However, as we found with the NLFFF extrapolation (Section 2.4), the shear angle around the sources of pulsations was high, reaching almost $\pi/2$ for some field lines, and the case with $\gamma = 0$ is unlikely to correspond to the flare studied. We will follow the way suggested by Inglis and Dennis (2012) to check the applicability of this mechanism to the flare studied. The ratio of the distance [D] between the centroids of the sources of adjacent pulsations along the PILs and period of pulsations [P] is related to the sound speed [v_s], the angle [α] between magnetic field and the maximum perpendicular group speed, and also to the shear angle [γ]. The analytical relation for the three cases looks as follows:

$$\frac{D}{P} = v_s \begin{cases} \sin\alpha, & \gamma = 0 \\ \sin\alpha/\cos\gamma, & 0 < \gamma < \pi/2 - \alpha \\ \cos\alpha/\sin\gamma, & \pi/2 - \alpha < \gamma < \pi/2 \end{cases}$$
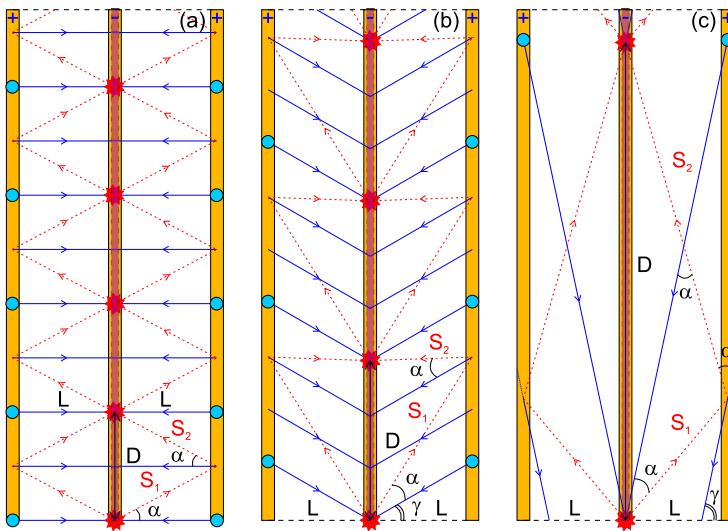
Figure 15 A scenario with the slow-mode waves as a propagating energy-release trigger in a three-ribbon flare. View from the top of the double magnetic arcade. Magnetic-field lines are shown by *blue solid lines with arrows*. The magnetic shear angle is γ. The flare ribbons are shown as *orange rectangles*. It is suggested that there is a null-line and/or current sheet in the corona (shown by the *red semitransparent dashed rectangle*) above the central flare ribbon. The propagation trajectories of slow-mode wave packets with the maximum group velocity perpendicular to the magnetic field (at an angle α) are shown by the *red dotted lines with arrows*. The regions of the interaction of the wave packets with the X-line, where episodes of the primary energy release and soft X-ray sources occur and where new wave packages are generated, are shown with the *red asterisks*. (**a**) Case: $\gamma = 0$, (**b**) case: $0 < \gamma < \pi/2 - \alpha$, and (**c**) case: $\pi/2 - \alpha < \gamma < \pi/2$. Blue circles – flare-loop footpoints where the strongest precipitation of non-thermal electrons and hard X-ray sources are expected. L is the distance from the loop footpoints to the X-line (roughly estimated as the distance between the adjacent flare ribbons), D is the distance between the sites of successive energy-release episodes, which can be estimated as the distance between centroids of the sources of successive X-ray pulsations. $S_1 + S_2$ is the path length traveled by the wave packet between two adjacent interactions with the X-line.

These solutions are shown in Figure 16 by the asterisks (for $\gamma = 0$), solid ($0 < \gamma < \pi/2 - \alpha$), and dashed ($\pi/2 - \alpha < \gamma < \pi/2$) curves. Here we took $\alpha = 28°$. The range of possible observed values for $\langle P \rangle = 54 \pm 13$ seconds, $\langle D \rangle = 1.8 \pm 1.0$ Mm, and several values of the sound speed, determined by the plasma temperature $T = 1, 3, 5, 10, 20, 30, 50, 100$ MK are shown with the filled horizontal rectangles with colors from black to white, respectively. One can see that the theoretical curves do not intersect with the range of possible values estimated from the observations in the physically reasonable range of plasma temperatures. This can indicate that this mechanism does not satisfy the observations of this flare. However, it should be noted that we made many simplifying assumptions, in particular: simplified two-dimensional geometry, homogeneity of all physical parameters in the flare region, the applicability of geometric optics (in particular, the angle of incidence of the wave is equal to the angle of reflection). The processes of initiation of magnetic reconnection by the waves, plasma heating, and electron acceleration are not considered at all. Realistic 3D simulations of this mechanism have not been carried out yet.

3.2.2. Asymmetric Rise of Curved and Twisted Field Lines

The asymmetric rise (eruption) of a twisted magnetic flux rope is considered as one of the possible mechanisms explaining the gradual propagation of the energy release (reconnec-
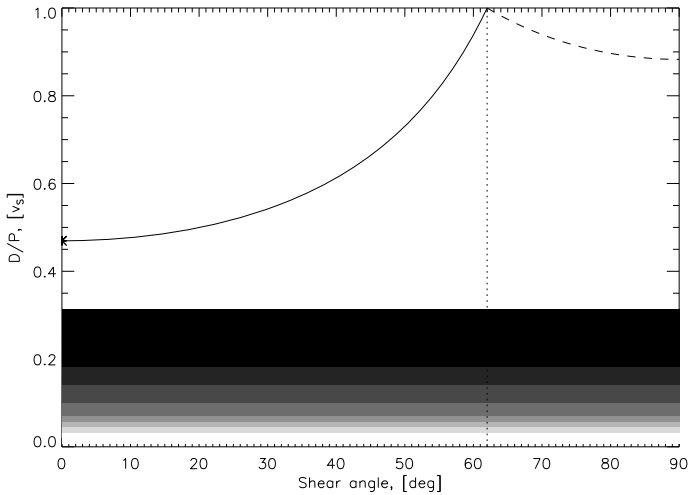
Figure 16 Dependence of the ratio of the distance between the sources of two adjacent QPPs [D] to their period [P] from the magnetic shear angle [γ] in the scenario where the slow-mode waves propagating at the angle $\alpha = 28°$ to the magnetic field serves as a trigger of reconnection (shown in Figure 15). The case $\gamma = 0$ is shown by the *asterisks*, the case $0 < \gamma < \pi/2 - \alpha$ – by the *solid curve*, and $\pi/2 - \alpha < \gamma < \pi/2$ – by the *dashed curve*. The D/P ratio (in units of the sound speed: v_s) obtained from the observations of the QPP sources for different plasma temperature $T = 1, 3, 5, 10, 20, 30, 50, 100$ MK is shown with the *shaded horizontal rectangles* (from *black to light gray*), the *vertical width* of which represents the estimated uncertainty.

tion) region and emission sources along the PILs in two-ribbon flares (e.g. Liu, Alexander, and Gilbert, 2009; Liu et al., 2010; Zimovets et al., 2018). However, recently Grechnev et al. (2020) showed that the interaction of an eruptive magnetic-flux rope with a coronal null-point (or a null-line) can lead to the formation of a current sheet, the reconnection in which can be the cause of three-ribbon flares. Although the M1.1 flare under study was not as powerful as the flares considered by Grechnev et al. (2020) and was not accompanied by a clear developed eruption, it had a similar magnetic geometry. Firstly, twisted magnetic-field lines of the western leg of the Ω-shaped loop system were located in the vicinity of the X-ray sources, and secondly, the coronal null-point was located in the immediate vicinity. Due to the curvature of the field lines of this leg (see Figure 13), a magnetic-tension force [F_t] directed along the normal upward and proportional to the square of the magnetic field and inversely proportional to the radius of curvature had to act on them.

A schematic illustration of a possible scenario is shown in Figure 17. Since the null-point was located slightly East of the source of the first pulsation, we can assume that the primary trigger of energy release occurred in the vicinity of this null-point. As a result, the curved field lines began to rise unevenly up along the central flare ribbon from East to West, leading to the uneven formation of a current sheet elongated from East to West. This process closely resembles the zipping-like asymmetric filament eruption illustrated in Figure 16 of Liu, Alexander, and Gilbert (2009). It can be assumed that the magnetic reconnection in this current sheet also progresses from East to West, which leads to the systematic motion of the X-ray source. The difference is that in our case, curved and twisted field lines could simultaneously penetrate two arcades – the south and the north ones. Such a magnetic structure could have formed, for example, as a result of partial reconnection of field lines during the numerous previous flares in this active region.
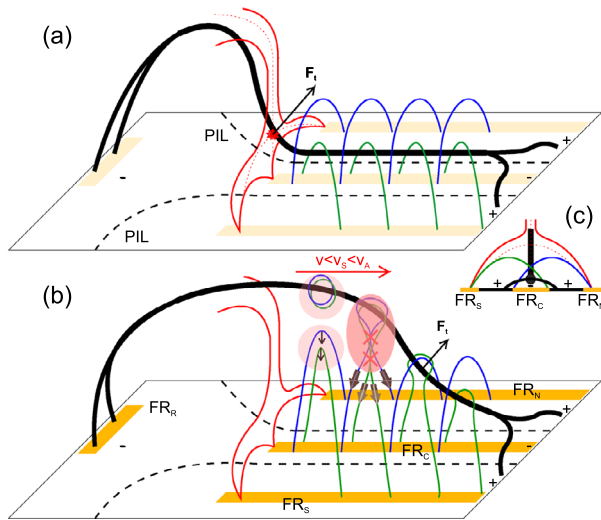
Figure 17 Illustration of a possible scenario of the M1.1 three-ribbon flare studied. (**a**) Magnetic configuration before the flare, (**b**) at some instant during the QPPs. (**c**) The pre-flare view from the right (west) end of the double arcade, which is shown by *blue and green* sheared loops. The curved magnetic-flux rope is shown in *bold black lines*. The field lines around the magnetic X-point in the corona are shown in *red*. The south (FR$_S$), central (FR$_C$), north (FR$_N$), and remote (FR$_R$) flare ribbons are shown by the *orange rectangles*. The positive and negative polarities of the magnetic field in the photosphere are indicated by the $+$ *and* $-$ *signs*, respectively. The PILs are shown by the *dashed curves*. The curved magnetic-flux rope rises unevenly due to the magnetic-tension force F_t from the *left* (from the East) to the *right* (West), which stretches the overlying magnetic-field lines and leads to their successive reconnection. This leads to sequential heating of the plasma (acceleration of particles) in various loops of the double arcade, QPPs, and the observed displacement (with the small velocity v) of their sources from East to West approximately above the central flare ribbon.

Two important questions are facing this scenario. The first one is why the energy release has a quasi-periodic character. The second one is why the displacement of the energy-release region is sub-sonic and sub-Alfvénic. We have no clear answers to these questions yet.

3.2.3. Flapping Oscillations of a Current Sheet

Artemyev and Zimovets ([2012](#)) proposed that QPPs and apparent motion of emission sources along the PIL in two-ribbon flares can be a consequence of the propagating flapping oscillations (waves) in a current sheet in the corona. In the antinodes of oscillations, the current density sharply increases, which could lead to a local anomalous increase in resistivity and more efficient reconnection, hence, plasma heating and particle acceleration. They found solutions for symmetric (sausage-like) unstable modes propagating in a current sheet with magnetic shear. This is important since the shear angle was probably very high in the flare studied.

Let us again suggest that there was a current sheet in the corona in the three-ribbon flare studied according to the scenario proposed by Wang et al. ([2014](#)) or it is formed due to an asymmetric rise of curved/twisted field lines. From Figure 2 of Artemyev and Zimovets ([2012](#)) one can infer that for the wavelet number $\lambda \approx d_{par} = 1.8 \pm 1.0 \approx 1$ Mm and angular frequency $\omega = 2\pi/P_{QPP} \approx 0.1$ s^{-1} of the oscillations, corresponding to the parameters found from the observations of the flare studied, there is a solution for a range of the dimensionless model parameter $\alpha \approx 10^{-6} - 10^{-4}$. This parameter $\alpha \approx B_z/B_{0y}$, where B_z is

the magnetic-field component in the stretched current sheet perpendicular to the PILs and B_{0y} is the equilibrium magnetic component in the current sheet along the PILs (see Figure 1 of Artemyev and Zimovets, 2012). These values of $\alpha \approx 10^{-4} - 10^{-6}$ look reasonable since we found that the shear angle could be very high (up to almost $90°$), and the B_z-component should be very small in the stretched reconnecting current sheet.

Let us now check at what parameters of the model the found unstable solution corresponds to the observed velocity of movement of the X-ray sources $v_{par} = 34 \pm 21$ km s^{-1} $\approx 10^4 - 10^5$ m s^{-1} (i.e. the wave group speed within the framework of the model). From Table 1 of Artemyev and Zimovets (2012), we get the dispersion relation for the considered mode-3: $\omega \approx b_m\,(v_A/L)\,(\alpha k/2\pi)^{1/2}$, where $b_m = B_{0y}/B_0$, v_A is the Alfvén speed, L is equilibrium current-sheet width, $k = 2\pi/\lambda$ is the wave number. B_0 is the undisturbed vertical magnetic field along the current-sheet boundaries. We obtain the group speed $v_{gr} = \partial\omega/\partial k \approx b_m\,(v_A/4\pi L)\,(\alpha\lambda)^{1/2}$. Since some parameters are unknown, let us make an estimate in order of magnitude. Remembering that we estimated $v_A \approx (0.94 - 26) \times 10^3$ km s^{-1}, let us take $v_A \approx 10^6 - 10^7$ m s^{-1}, $\alpha \approx 10^{-4} - 10^{-6}$, $\lambda \approx 10^6$ m (see above). Hence, $v_{gr} \approx (10^5 - 10^7) \times (B_{0y}/B_0)/L$ m s^{-1}. To satisfy $v_{gr} \approx v_{par} \approx 10^4 - 10^5$ m s^{-1}, we need that $(B_{0y}/B_0)/L \approx 10^{-3} - 10^0$ m^{-1}. The reconnecting current-sheet thickness can be assumed to be about several ion gyroradii $L \approx (10^{-1} - 10^0) \times T^{1/2}B^{-1}$ m, and under the broad ranges of plasma temperature from $T \approx 10^6$ K (ordinary corona) to $T \approx 10^8$ K (superhot plasma) and absolute magnetic-field value $B \approx 10^2 - 10^3$ G, we get $L \approx 10^{-1} - 10^3$ m. Hence, $B_{0y}/B_0 \approx 10^{-4} - 10^3$. It is a very broad range. Unfortunately, we are unable to estimate this ratio of the magnetic-field components in the current sheet from the observations and NLFFF extrapolation. With a high probability, the real ratio could be in this range.

Thus, we can conclude that this mechanism does not contradict observations. However, the large uncertainty in the physical parameters of the current sheet in the flare region, as well as the very simplified geometry of the model and the approximate nature of the solutions, do not allow us to draw more specific conclusions. In principle, the comparison of the predictions of this model with observations could be used to estimate some parameters of the flare current sheets if there were confidence that the mechanism really works in flares with moving sources of QPPs. This remark, however, is typical for most of the known QPP mechanisms (see discussion by Zimovets et al., 2021).

3.2.4. Thermal Instability of a Current Sheet

Recently, the theory of thermal instability in the pre-flare current sheet was developed in a series of works (Ledentsov, 2021a,b,c). Solutions were found for a wave-like disturbance propagating along the current and at a small angle to it for the cases of a neutral current sheet and a current sheet with a longitudinal magnetic-field component. It is shown that for the characteristic parameters of the corona in active regions, as a result of the thermal instability, the current sheet is fragmented along the current with a spatial period of $1 - 10$ Mm, which can decrease to $0.1 - 1.0$ Mm in the case of oblique propagation of the disturbance. Thus, in principle, this mechanism could explain the characteristic spatial scale $d_{par} = 1.8 \pm 1.0$ Mm between the sources of neighboring pulsations in the investigated flare. However, it is not clear whether this mechanism can explain the low speed of the systematic X-ray source motion along the current sheet since we were unable to find formulas for the velocities of propagation of the disturbance in these works. Ledentsov (2021b) also showed that a strong longitudinal magnetic field leads to spatial stabilization of the thermal instability (by the way, this is also valid for the flapping oscillations). Therefore, it is difficult to conclude to what extent this mechanism is applicable to the description of the considered flare, in which there was, most probably, a strong longitudinal component of the magnetic field.
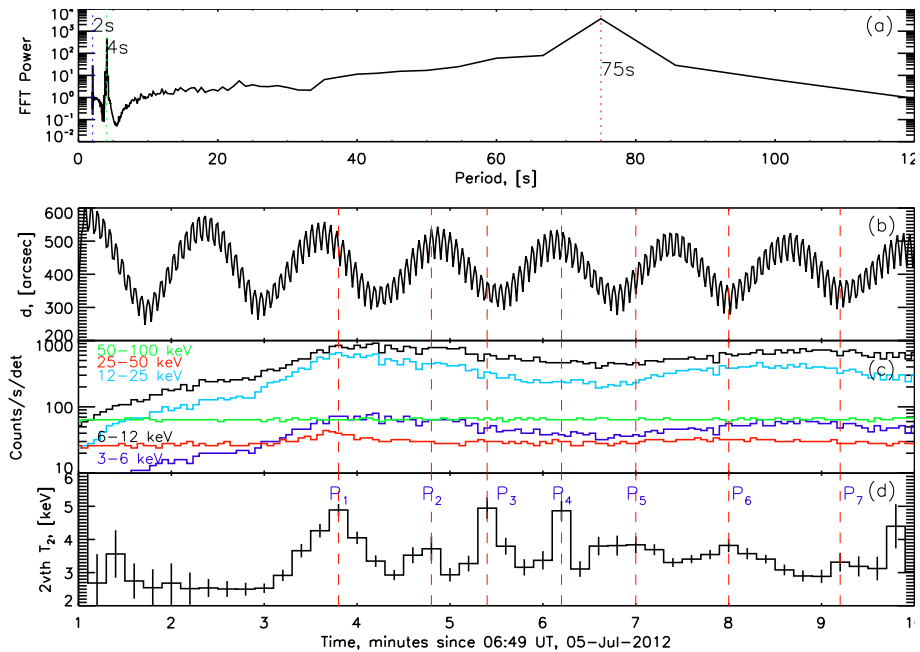
Figure 18 (**a**) Fourier spectrum of the smoothed temporal dependence of the angular distance between the RHESSI imaging-axis direction and the average position of the M1.1 flare studied. This temporal dependence smoothed over four seconds is shown in (**b**). Three spectral peaks with periods of 2, 4, and 75 seconds are indicated in (**a**) with *vertical dotted blue*, *green*, and *red lines*, respectively. (**c**) Count rates with the time step of four seconds averaged over the RHESSI's front detectors in five energy ranges $3-6$ (*dark blue*), $6-12$ (*black*), $12-25$ (*cyan*), $25-50$ (*red*), and $50-100$ (*green*) keV. (**d**) Temporal profile of the super-hot plasma temperature determined within the 2vth model. Peaks of pulsations $P_1 - P_7$ are shown with the *red vertical dashed lines* in (**b–d**).

4. Conclusion

We presented (as far as we know, for the first time) a detailed study of the quasi-periodic energy release in a three-ribbon solar flare. We found that the energy release took place in the form of quasi-periodic episodes, comparable in energy to a microflare, and the energy-release source was systematically moving at a low speed. These observations allowed us to discard a number of known mechanisms of QPPs and leave for consideration only a few of them, namely: i) the mechanism with slow magnetoacoustic waves, ii) asymmetric eruption, iii) flapping oscillations, and iv) thermal instability of a reconnecting current sheet. Analysis showed that slow magnetoacoustic waves were unlikely to trigger reconnection in the event studied. However, the level of available observational data and the sophistication of the models did not allow us to make an unambiguous choice from the last three mechanisms. We also cannot exclude the possibility that some other mechanism took place in the event considered. Further development of models and more detailed, spatially and spectrally resolved observations of sources of QPPs in solar flares are required.

Appendix

Here we address the question of whether the quasi-periodic variations (or QPPs) of the model parameters found from the X-ray spectra fitting could be a result of a known artifact
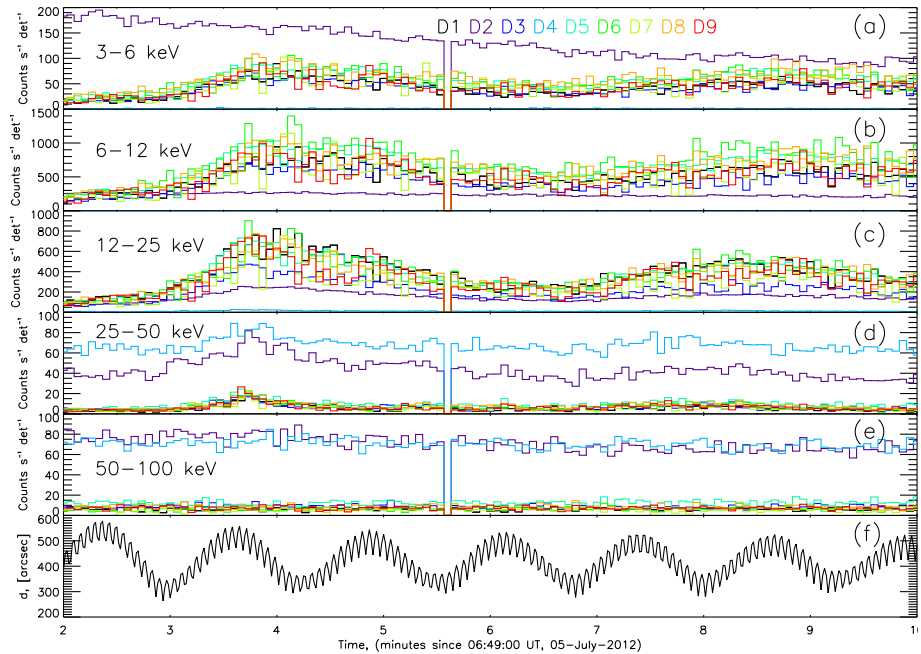
Figure 19 Count rates of RHESSI's front detectors D1, D2, . . ., D9 (shown by *different colors from black to red* and indicated on (**a**)) with temporal cadence of four seconds in five energy ranges: 3 – 6 (**a**), 6 – 12 (**b**), 12 – 25 (**c**), 25 – 50 (**d**), and 50 – 100 (**e**) keV. (**f**) The four-second smoothed time dependence of the angular distance between the RHESSI imaging-axis direction and the average position of the M1.1 flare studied.

in the RHESSI data. Inglis et al. (2011) found that count rates of the RHESSI detectors can contain artificial oscillations with period $P_{art} \approx 75$ seconds. In some flares, these oscillations are more pronounced, in others less so, or almost invisible. Since the period ($P_{QPP} = 54 \pm 13$ seconds) of the quasi-periodic variations is close to P_{art}, it makes sense to check whether they correspond to these artificial oscillations or not.

The RHESSI spacecraft rotates with a period of ≈ 4 seconds and experiences nutation. This motion produces oscillations of the telescope imaging axis with respect to the space-craft spin axis (these axes do not coincide with each other; see Fivian et al., 2002). The axis of each collimator deviates slightly from the imaging axis, and this deviation is different for different collimators. For Detector 5 (D5) the deviation is one of the largest, and hence the amplitude of the artificial-count rate oscillations of this detector can also be one of the largest (see Inglis et al., 2011).

Figure 18b shows the temporal profile of the angular distance [$d(t)$] between the RHESSI imaging-axis direction and the mean flare position in the image plane. It has a time step of one second, and it is smoothed over four seconds, i.e. about one period of the RHESSI rotation. The fast variations can be seen on top of the smoother sinusoidal varia-tions with an amplitude of about 250 arcseconds. The fast variations have a period of about four seconds and are a consequence of the rotation of the spacecraft, while longer variations have a period of about 75 seconds, i.e. around P_{art}, and they are a consequence of nutation. The Fourier spectrum of this signal is shown in Figure 18a, where one can see two sharp peaks corresponding to periods of about 2 and 4 seconds and one wider peak at about 75 sec-onds. For comparison, Figures 18c and 18d show the count rates averaged over the RHESSI

detectors and the temporal profile of the super-hot plasma temperature [$T_2(t)$] obtained in the 2vth model, respectively.

Overall, Figure 18 shows the following: i) unlike an almost sinusoidal signal $d(t)$ with a period $P_{art} \approx 75$ seconds, variations in $T_2(t)$ are unstable, i.e. have a variable period and amplitudes, ii) the temporal profiles $d(t)$ and $T_2(t)$ are not in phase, the peaks of $T_2(t)$ fall on different phases of the $d(t)$ oscillations, iii) no oscillations are seen in the averaged count rates of the RHESSI detectors. The oscillations with a period of $P_{art} \approx 75$ seconds are also not visible in the count rates of individual detectors D1, D2, . . . , D9 in different energy ranges from 3 to 100 keV (Figure 19). The oscillations are not even visible in the count rates of the D5 detector, for which the largest amplitude would be expected.

Thus, in the event under consideration, this artifact practically did not appear, and the arguments stated above oppose the possibility that the QPPs found may be a consequence of the artifact considered in the RHESSI data.

Data Availability The datasets generated during and/or analysed during the current study are available from the corresponding author on reasonable request.

Declarations

Disclosure of Potential Conflicts of Interest The authors declare that they have no conflict of interest.

References

Artemyev, A., Zimovets, I.: 2012, Stability of current sheets in the solar corona. *Solar Phys.* **277**, 283. DOI. ADS.

Aschwanden, M.J., Montello, M.L., Dennis, B.R., Benz, A.O.: 1995, Sequences of correlated hard X-ray and type III bursts during solar flares. *Astrophys. J.* **440**, 394. DOI. ADS.

Aulanier, G., Golub, L., DeLuca, E.E., Cirtain, J.W., Kano, R., Lundquist, L.L., Narukage, N., Sakao, T., Weber, M.A.: 2007, Slipping magnetic reconnection in coronal loops. *Science* **318**, 1588. DOI. ADS.

Benz, A.O.: 2017, Flare observations. *Liv. Rev. Solar Phys.* **14**, 2. DOI. ADS.

Benz, A.O., Monstein, C., Meyer, H., Manoharan, P.K., Ramesh, R., Altyntsev, A., Lara, A., Paez, J., Cho, K.-S.: 2009, A world-wide net of solar radio spectrometers: e-CALLISTO. *Earth Moon Planets* **104**, 277. DOI. ADS.

Bogachev, S.A., Somov, B.V., Kosugi, T., Sakao, T.: 2005, The motions of the hard X-ray sources in solar flares: images and statistics. *Astrophys. J.* **630**, 561. DOI. ADS.

Broomhall, A.-M., Davenport, J.R.A., Hayes, L.A., Inglis, A.R., Kolotkov, D.Y., McLaughlin, J.A., Mehta, T., Nakariakov, V.M., Notsu, Y., Pascoe, D.J., Pugh, C.E., Van Doorsselaere, T.: 2019, A blueprint of state-of-the-art techniques for detecting quasi-periodic pulsations in solar and stellar flares. *Astrophys. J. Suppl.* **244**, 44. DOI. ADS.

Brosius, J.W., Daw, A.N., Inglis, A.R.: 2016, Quasi-periodic fluctuations and chromospheric evaporation in a solar flare ribbon observed by Hinode/EIS, IRIS, and RHESSI. *Astrophys. J.* **830**, 101. DOI. ADS.

Brown, J.C.: 1973, The temperature structure of chromospheric flares heated by non-thermal electrons. *Solar Phys.* **31**, 143. DOI. ADS.

Caspi, A., Krucker, S., Lin, R.P.: 2014, Statistical properties of super-hot solar flares. *Astrophys. J.* **781**, 43. DOI. ADS.

Caspi, A., Lin, R.P.: 2010, RHESSI line and continuum observations of super-hot flare plasma. *Astrophys. J. Lett.* **725**, L161. DOI. ADS.

Chen, X., Yan, Y., Tan, B., Huang, J., Wang, W., Chen, L., Zhang, Y., Tan, C., Liu, D., Masuda, S.: 2019, Quasi-periodic Pulsations before and during a Solar Flare in AR 12242. *Astrophys. J.* **878**, 78. DOI. ADS.

Clarke, B.P., Hayes, L.A., Gallagher, P.T., Maloney, S.A., Carley, E.P.: 2021, Quasi-periodic particle acceleration in a solar flare. *Astrophys. J.* **910**, 123. DOI. ADS.

Dennis, B.R., Pernak, R.L.: 2009, Hard X-ray flare source sizes measured with the Ramaty High Energy Solar Spectroscopic Imager. *Astrophys. J.* **698**, 2131. DOI. ADS.

Dominique, M., Zhukov, A.N., Dolla, L., Inglis, A., Lapenta, G.: 2018, Detection of quasi-periodic pulsations in solar EUV time series. *Solar Phys.* **293**, 61. DOI. ADS.

Emslie, A.G., Dennis, B.R., Shih, A.Y., Chamberlin, P.C., Mewaldt, R.A., Moore, C.S., Share, G.H., Vourlidas, A., Welsch, B.T.: 2012, Global energetics of thirty-eight large solar eruptive events. *Astrophys. J.* **759**, 71. DOI. ADS.

Fivian, M., Hemmeck, R., McHedlishvili, A., Zehnder, A.: 2002, RHESSI aspect reconstruction. *Solar Phys.* **210**, 87. DOI. ADS.

Fletcher, L., Dennis, B.R., Hudson, H.S., Krucker, S., Phillips, K., Veronig, A., Battaglia, M., Bone, L., Caspi, A., Chen, Q., Gallagher, P., Grigis, P.T., Ji, H., Liu, W., Milligan, R.O., Temmer, M.: 2011, An observational overview of solar flares. *Space Sci. Rev.* **159**, 19. DOI. ADS.

Garcia, H.A.: 1994, Temperature and emission measure from goes soft X-ray measurements. *Solar Phys.* **154**, 275. DOI. ADS.

Grechnev, V.V., White, S.M., Kundu, M.R.: 2003, Quasi-periodic pulsations in a solar microwave burst. *Astrophys. J.* **588**, 1163. DOI. ADS.

Grechnev, V.V., Meshalkina, N.S., Uralov, A.M., Kochanov, A.A., Lesovoi, S.V., Myshyakov, I.I., Kiselev, V.I., Zhdanov, D.A., Altyntsev, A.T., Globa, M.V.: 2020, Twin null-point-associated major eruptive three-ribbon flares with unusual microwave spectra. *Solar Phys.* **295**, 128. DOI. ADS.

Grigis, P.C., Benz, A.O.: 2005, The evolution of reconnection along an arcade of magnetic loops. *Astrophys. J. Lett.* **625**, L143. DOI. ADS.

Gruszecki, M., Nakariakov, V.M.: 2011, Slow magnetacoustic waves in magnetic arcades. *Astron. Astrophys.* **536**, A68. DOI. ADS.

Hannah, I.G., Christe, S., Krucker, S., Hurford, G.J., Hudson, H.S., Lin, R.P.: 2008b, RHESSI microflare statistics. II. X-ray imaging, spectroscopy, and energy distributions. *Astrophys. J.* **677**, 704. DOI. ADS.

Hannah, I.G., Krucker, S., Hudson, H.S., Christe, S., Lin, R.P.: 2008a, An intriguing solar microflare observed with RHESSI, Hinode, and TRACE. *Astron. Astrophys.* **481**, L45. DOI. ADS.

Hannah, I.G., Hudson, H.S., Battaglia, M., Christe, S., Kašparová, J., Krucker, S., Kundu, M.R., Veronig, A.: 2011, Microflares and the statistics of X-ray flares. *Space Sci. Rev.* **159**, 263. DOI. ADS.

Hayes, L.A., Inglis, A.R., Christe, S., Dennis, B., Gallagher, P.T.: 2020, Statistical study of GOES X-ray quasi-periodic pulsations in solar flares. *Astrophys. J.* **895**, 50. DOI. ADS.

Holman, G.D., Aschwanden, M.J., Aurass, H., Battaglia, M., Grigis, P.C., Kontar, E.P., Liu, W., Saint-Hilaire, P., Zharkova, V.V.: 2011, Implications of X-ray observations for electron acceleration and propagation in solar flares. *Space Sci. Rev.* **159**, 107. DOI. ADS.

Hurford, G.J., Schmahl, E.J., Schwartz, R.A., Conway, A.J., Aschwanden, M.J., Csillaghy, A., Dennis, B.R., Johns-Krull, C., Krucker, S., Lin, R.P., McTiernan, J., Metcalf, T.R., Sato, J., Smith, D.M.: 2002, The RHESSI imaging concept. *Solar Phys.* **210**, 61. DOI. ADS.

Inglis, A.R., Dennis, B.R.: 2012, The relationship between hard X-ray pulse timings and the locations of footpoint sources during solar flares. *Astrophys. J.* **748**, 139. DOI. ADS.

Inglis, A.R., Zimovets, I.V., Dennis, B.R., Kontar, E.P., Nakariakov, V.M., Struminsky, A.B., Tolbert, A.K.: 2011, Instrumental oscillations in RHESSI count rates during solar flares. *Astron. Astrophys.* **530**, A47. DOI. ADS.

Inglis, A.R., Ireland, J., Dennis, B.R., Hayes, L., Gallagher, P.: 2016, A large-scale search for evidence of quasi-periodic pulsations in solar flares. *Astrophys. J.* **833**, 284. DOI. ADS.

Janvier, M., Aulanier, G., Démoulin, P.: 2015, From coronal observations to MHD simulations, the building blocks for 3D models of solar flares (invited review). *Solar Phys.* **290**, 3425. DOI. ADS.

Kashapova, L.K., Kupriyanova, E.G., Xu, Z., Reid, H.A.S., Kolotkov, D.Y.: 2020, The origin of quasi-periodicities during circular ribbon flares. *Astron. Astrophys.* **642**, A195. DOI. ADS.

Kim, S., Masuda, S., Shibasaki, K., Bong, S.-C.: 2013, Systematic microwave source motions along a flare-arcade observed by Nobeyama Radioheliograph and AIA/SDO. *Publ. Astron. Soc. Japan* **65**, S2. DOI. ADS.

Kumar, P., Nakariakov, V.M., Cho, K.-S.: 2016, Observation of a quasiperiodic pulsation in hard X-ray, radio, and extreme-ultraviolet wavelengths. *Astrophys. J.* **822**, 7. DOI. ADS.

Kupriyanova, E.G., Kashapova, L.K., Reid, H.A.S., Myagkova, I.N.: 2016, Relationship of type III radio bursts with quasi-periodic pulsations in a solar flare. *Solar Phys.* **291**, 3427. DOI. ADS.

Kupriyanova, E., Kolotkov, D., Nakariakov, V., Kaufman, A.: 2020, Quasi-periodic pulsations in solar and stellar flares. Review. *J. Solar-Terr. Phys.* **6**, 3. DOI. ADS.

Kuznetsov, S.A., Zimovets, I.V., Morgachev, A.S., Struminsky, A.B.: 2016, Spatio-temporal dynamics of sources of hard X-ray pulsations in solar flares. *Solar Phys.* **291**, 3385. DOI. ADS.

Kuznetsov, S.A., Zimovets, I.V., Melnikov, V.F., Wang, R.: 2017, Spatio-temporal evolution of sources of microwave and hard X-ray pulsations of the solar flare using the NoRH, RHESSI, and AIA/SDO observation data. *Geomagn. Aeron.* **57**, 1067. DOI. ADS.

Ledentsov, L.: 2021a, Thermal trigger for solar flares I: fragmentation of the preflare current layer. *Solar Phys.* **296**, 74. DOI. ADS.

Ledentsov, L.: 2021b, Thermal trigger for solar flares II: effect of the guide magnetic field. *Solar Phys.* **296**, 93. DOI. ADS.

Ledentsov, L.: 2021c, Thermal trigger for solar flares III: effect of the oblique layer fragmentation. *Solar Phys.* **296**, 117. DOI. ADS.

Ledentsov, L.S., Somov, B.V.: 2016, Thermal instability of the reconnecting current layer in solar flares. *Astron. Lett.* **42**, 841. DOI. ADS.

Lemen, J.R., Title, A.M., Akin, D.J., Boerner, P.F., Chou, C., Drake, J.F., Duncan, D.W., Edwards, C.G., Friedlaender, F.M., Heyman, G.F., Hurlburt, N.E., Katz, N.L., Kushner, G.D., Levay, M., Lindgren, R.W., Mathur, D.P., McFeaters, E.L., Mitchell, S., Rehse, R.A., Schrijver, C.J., Springer, L.A., Stern, R.A., Tarbell, T.D., Wuelser, J.-P., Wolfson, C.J., Yanari, C., Bookbinder, J.A., Cheimets, P.N., Caldwell, D., Deluca, E.E., Gates, R., Golub, L., Park, S., Podgorski, W.A., Bush, R.I., Scherrer, P.H., Gummin, M.A., Smith, P., Auker, G., Jerram, P., Pool, P., Soufli, R., Windt, D.L., Beardsley, S., Clapp, M., Lang, J., Waltham, N.: 2012, The Atmospheric Imaging Assembly (AIA) on the Solar Dynamics Observatory (SDO). *Solar Phys.* **275**, 17. DOI. ADS.

Li, D., Ning, Z.J., Zhang, Q.M.: 2015, Imaging and spectral observations of quasi-periodic pulsations in a solar flare. *Astrophys. J.* **807**, 72. DOI. ADS.

Li, T., Zhang, J.: 2015, Quasi-periodic slipping magnetic reconnection during an X-class solar flare observed by the Solar Dynamics Observatory and Interface Region Imaging Spectrograph. *Astrophys. J. Lett.* **804**, L8. DOI. ADS.

Li, D., Kolotkov, D.Y., Nakariakov, V.M., Lu, L., Ning, Z.J.: 2020, Quasi-periodic pulsations of gamma-ray emissions from a solar flare on 2017 September 6. *Astrophys. J.* **888**, 53. DOI. ADS.

Lin, R.P., Dennis, B.R., Hurford, G.J., Smith, D.M., Zehnder, A., Harvey, P.R., Curtis, D.W., Pankow, D., Turin, P., Bester, M., Csillaghy, A., Lewis, M., Madden, N., van Beek, H.F., Appleby, M., Raudorf, T., McTiernan, J., Ramaty, R., Schmahl, E., Schwartz, R., Krucker, S., Abiad, R., Quinn, T., Berg, P., Hashii, M., Sterling, R., Jackson, R., Pratt, R., Campbell, R.D., Malone, D., Landis, D., Barrington-Leigh, C.P., Slassi-Sennou, S., Cork, C., Clark, D., Amato, D., Orwig, L., Boyle, R., Banks, I.S., Shirey, K., Tolbert, A.K., Zarro, D., Snow, F., Thomsen, K., Henneck, R., McHedlishvili, A., Ming, P., Fivian, M., Jordan, J., Wanner, R., Crubb, J., Preble, J., Matranga, M., Benz, A., Hudson, H., Canfield, R.C., Holman, G.D., Crannell, C., Kosugi, T., Emslie, A.G., Vilmer, N., Brown, J.C., Johns-Krull, C., Aschwanden, M., Metcalf, T., Conway, A.: 2002, The Reuven Ramaty High-Energy Solar Spectroscopic Imager (RHESSI). *Solar Phys.* **210**, 3. DOI. ADS.

Liu, R., Alexander, D., Gilbert, H.R.: 2009, Asymmetric eruptive filaments. *Astrophys. J.* **691**, 1079. DOI. ADS.

Liu, W., Petrosian, V., Dennis, B.R., Jiang, Y.W.: 2008, Double coronal hard and soft X-ray source observed by RHESSI: evidence for magnetic reconnection and particle acceleration in solar flares. *Astrophys. J.* **676**, 704. DOI. ADS.

Liu, C., Lee, J., Jing, J., Liu, R., Deng, N., Wang, H.: 2010, Motions of hard X-ray sources during an asymmetric eruption. *Astrophys. J. Lett.* **721**, L193. DOI. ADS.

Masson, S., Pariat, E., Aulanier, G., Schrijver, C.J.: 2009, The nature of flare ribbons in coronal null-point topology. *Astrophys. J.* **700**, 559. DOI. ADS.

McLaughlin, J.A., Nakariakov, V.M., Dominique, M., Jelínek, P., Takasao, S.: 2018, Modelling quasi-periodic pulsations in solar and stellar flares. *Space Sci. Rev.* **214**, 45. DOI. ADS.

Nakariakov, V.M., Melnikov, V.F.: 2009, Quasi-periodic pulsations in solar flares. *Space Sci. Rev.* **149**, 119. DOI. ADS.

Nakariakov, V.M., Zimovets, I.V.: 2011, Slow magnetoacoustic waves in two-ribbon flares. *Astrophys. J. Lett.* **730**, L27. DOI. ADS.

Nakariakov, V.M., Inglis, A.R., Zimovets, I.V., Foullon, C., Verwichte, E., Sych, R., Myagkova, I.N.: 2010, Oscillatory processes in solar flares. *Plasma Phys. Control. Fusion* **52**, 124009. DOI. ADS.

Nakariakov, V.M., Pilipenko, V., Heilig, B., Jelínek, P., Karlický, M., Klimushkin, D.Y., Kolotkov, D.Y., Lee, D.-H., Nisticò, G., Van Doorsselaere, T., Verth, G., Zimovets, I.V.: 2016, Magnetohydrodynamic

oscillations in the solar corona and Earth's magnetosphere: towards consolidated understanding. *Space Sci. Rev.* **200**, 75. DOI. ADS.

Pariat, E., Antiochos, S.K., DeVore, C.R.: 2010, Three-dimensional modeling of quasi-homologous solar jets. *Astrophys. J.* **714**, 1762. DOI. ADS.

Priest, E.R., Forbes, T.G.: 2002, The magnetic nature of solar flares. *Astron. Astrophys. Rev.* **10**, 313. DOI. ADS.

Pugh, C.E., Broomhall, A.-M., Nakariakov, V.M.: 2019, Scaling laws of quasi-periodic pulsations in solar flares. *Astron. Astrophys.* **624**, A65. DOI. ADS.

Pugh, C.E., Nakariakov, V.M., Broomhall, A.-M., Bogomolov, A.V., Myagkova, I.N.: 2017, Properties of quasi-periodic pulsations in solar flares from a single active region. *Astron. Astrophys.* **608**, A101. DOI. ADS.

Qiu, J., Longcope, D.W., Cassak, P.A., Priest, E.R.: 2017, Elongation of flare ribbons. *Astrophys. J.* **838**, 17. DOI. ADS.

Reid, H.A.S., Ratcliffe, H.: 2014, A review of solar type III radio bursts. *Res. Astron. Astrophys.* **14**, 773. DOI. ADS.

Rudenko, G.V., Myshyakov, I.I.: 2009, Analysis of reconstruction methods for nonlinear force-free fields. *Solar Phys.* **257**, 287. DOI. ADS.

Scherrer, P.H., Schou, J., Bush, R.I., Kosovichev, A.G., Bogart, R.S., Hoeksema, J.T., Liu, Y., Duvall, T.L., Zhao, J., Title, A.M., Schrijver, C.J., Tarbell, T.D., Tomczyk, S.: 2012, The Helioseismic and Magnetic Imager (HMI) investigation for the Solar Dynamics Observatory (SDO). *Solar Phys.* **275**, 207. DOI. ADS.

Schrijver, C.J., DeRosa, M.L., Metcalf, T., Barnes, G., Lites, B., Tarbell, T., McTiernan, J., Valori, G., Wiegelmann, T., Wheatland, M.S., Amari, T., Aulanier, G., Démoulin, P., Fuhrmann, M., Kusano, K., Régnier, S., Thalmann, J.K.: 2008, Nonlinear force-free field modeling of a solar active region around the time of a major flare and coronal mass ejection. *Astrophys. J.* **675**, 1637. DOI. ADS.

Schwartz, R.A., Csillaghy, A., Tolbert, A.K., Hurford, G.J., McTiernan, J., Zarro, D.: 2002, RHESSI data analysis software: rationale and methods. *Solar Phys.* **210**, 165. DOI. ADS.

Sharykin, I.N., Struminskii, A.B., Zimovets, I.V.: 2015, Plasma heating to super-hot temperatures (>30 MK) in the August 9, 2011 solar flare. *Astron. Lett.* **41**, 53. DOI. ADS.

Sharykin, I.N., Zimovets, I.V., Myshyakov, I.I.: 2020, Flare energy release at the magnetic field polarity inversion line during the M1.2 solar flare of 2015 March 15. II. Investigation of photospheric electric current and magnetic field variations using HMI 135 s vector magnetograms. *Astrophys. J.* **893**, 159. DOI. ADS.

Sharykin, I.N., Struminsky, A.B., Zimovets, I.V., Gan, W.-Q.: 2016, Solar flares with similar soft but different hard X-ray emissions: case and statistical studies. *Res. Astron. Astrophys.* **16**, 5. DOI. ADS.

Sharykin, I.N., Zimovets, I.V., Myshyakov, I.I., Meshalkina, N.S.: 2018, Flare energy release at the magnetic field polarity inversion line during the M1.2 solar flare of 2015 March 15. I. Onset of plasma heating and electron acceleration. *Astrophys. J.* **864**, 156. DOI. ADS.

Shibata, K., Magara, T.: 2011, Solar flares: magnetohydrodynamic processes. *Liv. Rev. Solar Phys.* **8**, 6. DOI. ADS.

Simões, P.J.A., Hudson, H.S., Fletcher, L.: 2015, Soft X-ray pulsations in solar flares. *Solar Phys.* **290**, 3625. DOI. ADS.

Smith, D.M., Lin, R.P., Turin, P., Curtis, D.W., Primbsch, J.H., Campbell, R.D., Abiad, R., Schroeder, P., Cork, C.P., Hull, E.L., Landis, D.A., Madden, N.W., Malone, D., Pehl, R.H., Raudorf, T., Sangsingkeow, P., Boyle, R., Banks, I.S., Shirey, K., Schwartz, R.: 2002, The RHESSI spectrometer. *Solar Phys.* **210**, 33. DOI. ADS.

Song, Y.L., Tian, H., Zhang, M., Ding, M.D.: 2018, Observations of white-light flares in NOAA active region 11515: high occurrence rate and relationship with magnetic transients. *Astron. Astrophys.* **613**, A69. DOI. ADS.

Sui, L., Holman, G.D.: 2003, Evidence for the formation of a large-scale current sheet in a solar flare. *Astrophys. J. Lett.* **596**, L251. DOI. ADS.

Sun, X., Hoeksema, J.T., Liu, Y., Aulanier, G., Su, Y., Hannah, I.G., Hock, R.A.: 2013, Hot spine loops and the nature of a late-phase solar flare. *Astrophys. J.* **778**, 139. DOI. ADS.

Tsuneta, S., Ichimoto, K., Katsukawa, Y., Nagata, S., Otsubo, M., Shimizu, T., Suematsu, Y., Nakagiri, M., Noguchi, M., Tarbell, T., Title, A., Shine, R., Rosenberg, W., Hoffmann, C., Jurcevich, B., Kushner, G., Levay, M., Lites, B., Elmore, D., Matsushita, T., Kawaguchi, N., Saito, H., Mikami, I., Hill, L.D., Owens, J.K.: 2008, The Solar Optical Telescope for the Hinode mission: an overview. *Solar Phys.* **249**, 167. DOI. ADS.

Van Doorsselaere, T., Kupriyanova, E.G., Yuan, D.: 2016, Quasi-periodic pulsations in solar and stellar flares: an overview of recent results (invited review). *Solar Phys.* **291**, 3143. DOI. ADS.

Veronig, A.M., Brown, J.C.: 2004, A coronal thick-target interpretation of two hard X-ray loop events. *Astrophys. J. Lett.* **603**, L117. DOI. ADS.

Vorpahl, J.A.: 1976, The triggering and subsequent development of a solar flare. *Astrophys. J.* **205**, 868. DOI. ADS.

Wang, H., Liu, C., Deng, N., Zeng, Z., Xu, Y., Jing, J., Cao, W.: 2014, Study of two successive three-ribbon solar flares on 2012 July 6. *Astrophys. J. Lett.* **781**, L23. DOI. ADS.

Wheatland, M.S., Sturrock, P.A., Roumeliotis, G.: 2000, An optimization approach to reconstructing force-free fields. *Astrophys. J.* **540**, 1150. DOI. ADS.

Zhang, Q.M., Li, D., Ning, Z.J.: 2016, Chromospheric condensation and quasi-periodic pulsations in a circular-ribbon flare. *Astrophys. J.* **832**, 65. DOI. ADS.

Zimovets, I.V., Sharykin, I.N., Gan, W.Q.: 2020, Relationships between photospheric vertical electric currents and hard X-ray sources in solar flares: statistical study. *Astrophys. J.* **891**, 138. DOI. ADS.

Zimovets, I.V., Struminsky, A.B.: 2009, Imaging observations of quasi-periodic pulsatory nonthermal emission in two-ribbon solar flares. *Solar Phys.* **258**, 69. DOI. ADS.

Zimovets, I.V., Struminsky, A.B.: 2010, Observations of double-periodic X-ray emission in interacting systems of solar flare loops. *Solar Phys.* **263**, 163. DOI. ADS.

Zimovets, I.V., Wang, R., Liu, Y.D., Wang, C., Kuznetsov, S.A., Sharykin, I.N., Struminsky, A.B., Nakariakov, V.M.: 2018, Magnetic structure of solar flare regions producing hard X-ray pulsations. *J. Atmos. Solar-Terr. Phys.* **174**, 17. DOI. ADS.

Zimovets, I.V., McLaughlin, J.A., Srivastava, A.K., Kolotkov, D.Y., Kuznetsov, A.A., Kupriyanova, E.G., Cho, I.-H., Inglis, A.R., Reale, F., Pascoe, D.J., Tian, H., Yuan, D., Li, D., Zhang, Q.M.: 2021, Quasi-periodic pulsations in solar and stellar flares: a review of underpinning physical mechanisms and their predicted observational signatures. *Space Sci. Rev.* **217**, 66. DOI. ADS.

Authors and Affiliations

Ivan Zimovets[1] · **Ivan Sharykin[1]** · **Ivan Myshyakov[2]**

✉ I. Zimovets
ivanzim@iki.rssi.ru

1   Space Research Institute of the Russian Academy of Sciences (IKI RAS), Profsoyuznaya St. 84/32, Moscow, 117997, Russia

2   Institute of Solar-Terrestrial Physics, Siberian Branch of the Russian Academy of Sciences (ISTP SB RAS), Lermontov St. 126A, Irkutsk, 664033, Russia